IDEA League

Master of Science in Applied Geophysics

Research Thesis

Towards sparse seismic acquisition with AUVs: improving underwater navigation and full wavefield migration of seismic and AUV data

Nicolas Morandini

August 9, 2018

Towards sparse seismic acquisition with AUVs: improving underwater navigation and full wavefield migration of seismic and AUV data

Master of Science Thesis

for the degree of Master of Science in Applied Geophysics at
Delft University of Technology
ETH Zürich
RWTH Aachen University
by

Nicolas Morandini

August 9, 2018

Department of Geoscience & Engineering · Delft University of Technology
Department of Earth Sciences · ETH Zürich
Faculty of Georesources and Material Engineering · RWTH Aachen University

Delft University of Technology

Printed in The Netherlands, Switzerland, Germany

IDEA LEAGUE
JOINT MASTER'S IN APPLIED GEOPHYSICS

Delft University of Technology, The Netherlands
ETH Zürich, Switzerland
RWTH Aachen, Germany

Dated: *August 9, 2018*

Committee Members:

Prof. Dr. Florian Wellmann

Dr. Gerrit Blacquière

Supervisor(s):

Dr. Ir. G.J.A. van Groenestijn

Dr. Gerrit Blacquière

Abstract

This thesis demonstrates, that bathymetric data improves data imaging results of full wavefield migration using different acquisition designs. The algorithm gets more stable by constraining the inversion with the sea bottom information, especially in case of large source and receiver spacings, without making compromises on image quality. Not using the proposed method will result in uninterpretable images, if the topography of the seafloor gets too complex.

In this thesis it is proposed to use an autonomous underwater vehicle (AUV) to acquire the bathymetry. The quality of the bathymetry is highly dependent on the ability to adequately localize the AUV. Therefore a terrain based navigation system was developed based on Kalman filters. It is shown that using a Kalman filter combined with sparsely sampled sea bottom information was of advantage to locate the vehicle at its true position. This is not possible with just using the inertial navigation system of the AUV.

Acknowledgements

This project was conducted in cooperation with TU Delft and TNO.

I want to express my deepest gratitude to the people who contributed to my thesis. I especially want to thank Gert-Jan van Groenestijn for his guiding and intensive work he put into the supervision. Also, I want to express my deepest appreciation to Gerrit Blacquière and Peter Beerens for the given advice, discussions and remarks on my work and writings.

Furthermore I want to thank the management of TNO for giving me the opportunity to work at this exciting project, and Delphi Consortium for giving me the chance to use the full wavefield migration software and therefore getting an insight into the algorithm.

Last but not least I want to thank my parents for all the support during the last 6 years.

Delft University of Technology
August 9, 2018

Nicolas Morandini

Table of Contents

Acronyms

AUV	Autonomous underwater vehicle
FWI	Full waveform inversion
FWM	Full wavefield migration
GPS	Global positioning system
INS	Inertial navigation system
ISSS	Interferometric side scan sonar
MBES	Multi-beam echo sounder
SSS	Side-scan sonar
TBN	Terrain based navigation

Chapter 1

Introduction

Towards sparse aquisition with AUVs deals with the question if autonomous underwater vehicles (AUVs) can be of value for the seismic industry. In this work, we want to explore if data regarding the sea bottom topography coming from AUVs can be of aid to the newest state of the art depth imaging algorithm called full wavefield migration (Figure 1-1).

Full wavefield migration [Berkhout and Verschuur, 2011] is a recently developed depth imaging technique. It includes multiple scattering effects into the imaging process by inverting for a model of reflectivity in depth. Therefore multiples, in conventional imaging techniques considered as noise, are hereby considered as signal which are accounted for in the modeling using propagation and reflection operators. Nevertheless inversion based algorithms are always of uncertain nature, prone to local minima and the end result is often dependent on apriori information. The apriori information can be used to constrain the inversion leading to the desired approximate of the truth. In this work we consider the case of seismic data acquired in a marine environment with a complex sea bottom topography. We analyze how this environment will effect the inversion results and how bathymetric data acquired by autonomous underwater vehicles can be beneficial in order to create a clean seismic image of the subsurface. Furthermore we observe the proposed method for different acquisition settings with different sampling of sources as well as receivers along the surface.

To make AUVs beneficial for seismic surveys, the bathymetric data has to be of good quality which is highly dependent on the accuracy of the depth measurement as well as the accuracy of the positioning of the vehicle. Since underwater the global positioning system (GPS) signal is not available, it is a big challenge to relate depth measurements to correct spacial coordinates. Therefore an accurate navigation system is inevitable to create high quality sea bottom maps for the seismic industry but also for other industries from military to construction. We not only use the sensor data, but also the measured depth information and thereby create a more accurate positioning method of the AUV.

This work is structured into a general introduction (*Chapter 1*), a section concerning the AUV navigation system (*Chapter 2*) and a section regarding how to implement AUV data into full wavefield migration (*Chapter 3*). Last but not least, a final conclusion is given (*Chapter 4*). *Chapter 2* and *Chapter 3* can be read separately from each other.

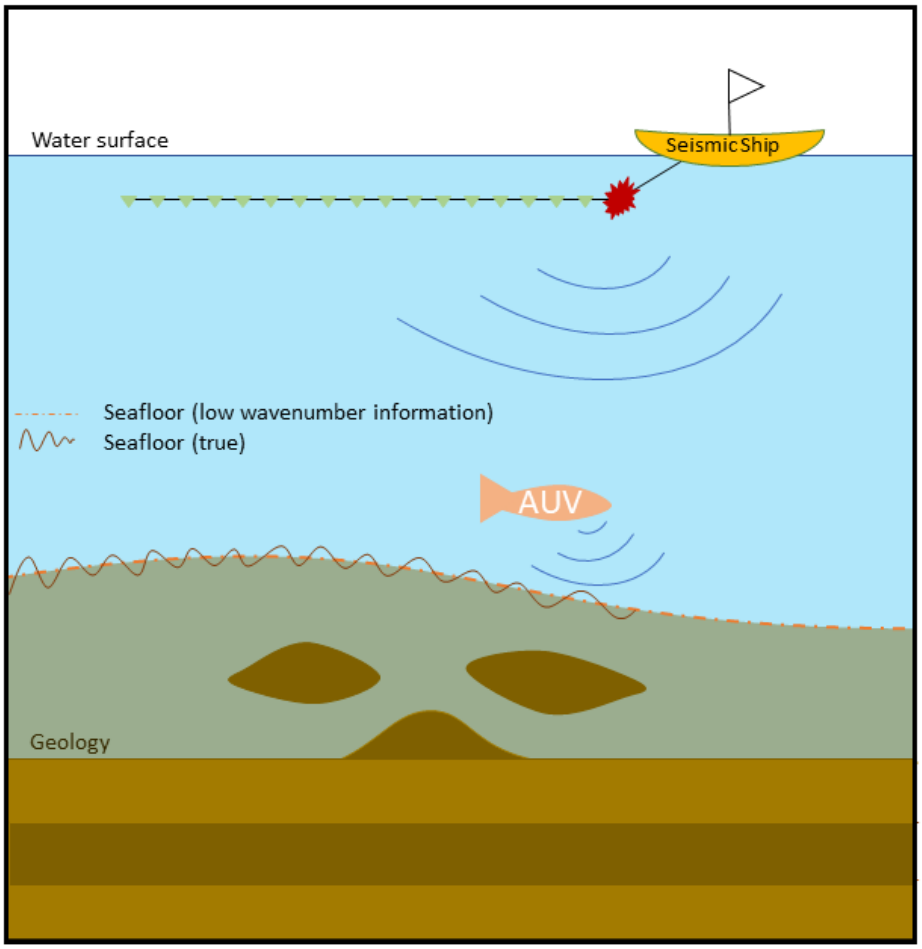

Figure 1-1: An AUV maps the sea floor during a seismic survey

Chapter 2

AUV Navigation

2-1 Introduction

AUVs are widely used by various industries, scientific institutions and military organizations in order to perform tasks from inspecting steel constructions underwater to creating bathymetric maps. Just recently AUVs started being used for deploying ocean bottom nodes on the seafloor, for ocean bottom seismic surveys to perform reservoir monitoring tasks [Tsingas et al., 2017]. Like mentioned in *Chapter 1*, especially for mapping tasks the knowledge regarding the position of the vehicle is an essential requirement since it is of high importance to assign the measurement quantities, in our case the specific depth levels, to the right coordinates. Unfortunately we cannot rely on GPS measurements as underwater GPS signals cannot be received [Taraldsen et al., 2011]. This leads to the fact that the AUV has to frequently be brought back to the sea surface to re-calibrate its actual position. We try to improve the positioning of the AUV by making advantage of its sonar system used during the mapping process itself. Therefore we consider the case of already existing sparse sea bottom data, acquired by surface vessels or seismic surveys.

In this chapter we first give an introduction on the theory of Kalman filter based navigation (section 2-2). Secondly an explanation of the terrain based navigation algorithm is given (section 2-3), followed by the results achieved (section 2-5).

2-1-1 AUV sonar sensors

Several sonar systems are available today, applied for various types of applications. One system is the multi-beam echo sounder (MBES) [Hammerstad et al., 1993] which is mostly deployed by surface vessels. It transmits a narrow acoustic pulse from the ocean surface to the sea bottom and makes statements regarding the water depth by listening to the reflections.

Another type of sonar system is the side-scan sonar (SSS) [Glynn and Buffman, 1996] which has the main purpose of illuminating the seabed to detect objects and is mainly used by AUVs. This is done by transmitting a beam typically 45° wide, perpendicular to the sailing

direction of the vehicle. Conventional side-scan sonars cannot measure absolute water depth due to single acoustic sensors receiving the reflected signal.

If one wants to record the water depth using a side-scan, an interferometric side-scan sonar (ISSS) [Sintes, 2002] has to be applied which works with multiple separated sensors in an array. The depth can be calculated by determining the direction of the reflection point in combination with the arrival times at the receivers. In this work we assume to operate an AUV using ISSS with a beam illumination of 45° which goes perpendicular to the sailing direction.

2-2 Kalman filter based navigation

2-2-1 States, predictions and measurements

The Kalman filter introduced by [Kalman, 1960], is a recursive algorithm which combines information to make estimates of a system. The Kalman filter is a valuable tool if measurements are available from sensors and the system can simultaneously be described by mathematical models. In this work a Kalman filter was set up as the best possible estimator for underwater navigation which combines sensor data from the underwater vehicle with data acquired by the vehicle regarding the underlying topography. This is done while taking into account the uncertainties of the system which have to be quantified. For the case discussed in this work, the state $\vec{x}_{s_t}$ of the to be located AUV would the position (x, y, z), as well as the operating velocity (v_x, v_y, v_z):

$$\vec{x}_{s_t} = \begin{bmatrix} x \\ y \\ z \\ v_x \\ v_y \\ v_z \end{bmatrix} \tag{2-1}$$

To make a prediction for the position and velocity at $t + dt$ we can make use of the kinematic equations. To do so, a state prediction matrix F is set up which converts the state at time step t to a prediction at time $t + dt$:

$$\mathbf{F} = \begin{bmatrix} 1 & 0 & 0 & dt & 0 & 0 \\ 0 & 1 & 0 & 0 & dt & 0 \\ 0 & 0 & 1 & 0 & 0 & dt \\ 0 & 0 & 0 & 1 & 0 & 0 \\ 0 & 0 & 0 & 0 & 1 & 0 \\ 0 & 0 & 0 & 0 & 0 & 1 \end{bmatrix} \tag{2-2}$$

By multiplying the state prediction matrix $\mathbf{F}$ with the state vector $\vec{x}_{s_t}$, a prediction $\vec{x}_{p_{t+dt}}$ can be made of position and velocity at time $t + dt$:

$$\vec{x}_{p_{t+dt}} = \mathbf{F}\vec{x}_{s_t} \tag{2-3}$$

This predicted state will later on be compared with the data received from sensors of the AUV. The data $\vec{z}_{t+dt}$ is stored in a vector that in our case has the same dimensions as the predicted state:

$$\vec{z}_{t+dt} = \begin{bmatrix} x \\ y \\ z \\ v_x \\ v_y \\ v_z \end{bmatrix} \tag{2-4}$$

The concept of states, predictions and measurements is visualized in Figure 2-1.

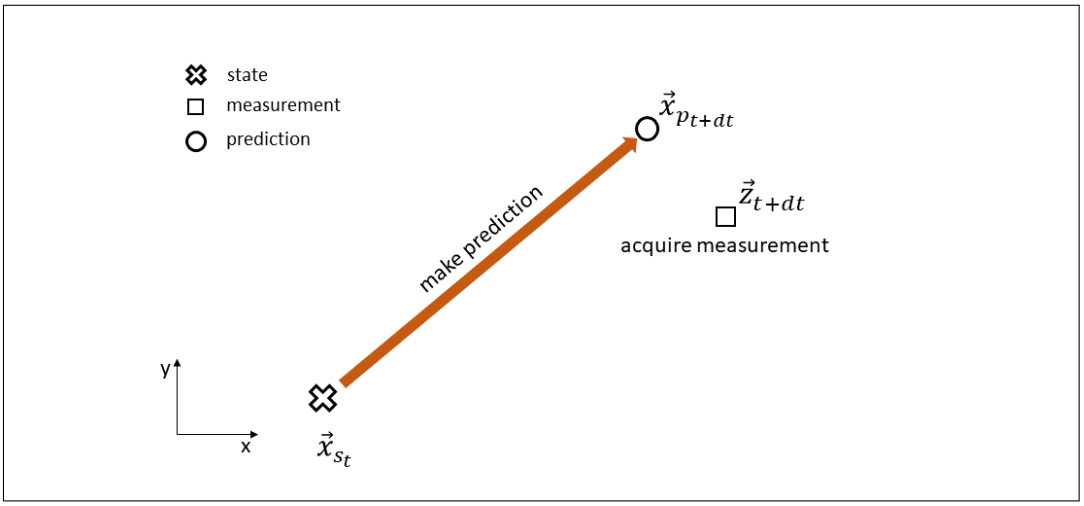

Figure 2-1: States, measurements and predictions

The question is given the prediction $\vec{x}_{p_{t+dt}}$ and measurement $\vec{z}_{t+dt}$, where to position $\vec{x}_{s_{t+dt}}$. In order to answer this question, uncertainties in the prediction as well as the accuracies of the measurements have to be quantified.

2-2-2 State uncertainties, prediction uncertainties and measurement accuracies

To describe uncertainties and accuracies in the system, covariance matrices are used. Thereby we use the term accuracies related to measurements and uncertainties related to predictions and the state. Covariance matrices are not only describing the variances of the states but also how the different states depend on each other. In our three dimensional case, the covariance matrix can be defined as follows:

$$\sum_{ij} = \begin{bmatrix} \sigma_{xx} & \sigma_{xy} & \sigma_{xz} & \sigma_{xv_x} & \sigma_{xv_y} & \sigma_{xv_z} \\ \sigma_{yx} & \sigma_{yy} & \sigma_{yz} & \sigma_{yv_x} & \sigma_{yv_y} & \sigma_{yv_z} \\ \sigma_{zx} & \sigma_{zy} & \sigma_{zz} & \sigma_{zv_x} & \sigma_{zv_y} & \sigma_{zv_z} \\ \sigma_{v_x x} & \sigma_{v_x y} & \sigma_{v_x z} & \sigma_{v_x v_x} & \sigma_{v_x v_y} & \sigma_{v_x v_z} \\ \sigma_{v_y x} & \sigma_{v_y y} & \sigma_{v_y z} & \sigma_{v_y v_x} & \sigma_{v_y v_y} & \sigma_{v_y v_z} \\ \sigma_{v_z x} & \sigma_{v_z y} & \sigma_{v_z z} & \sigma_{v_z v_x} & \sigma_{v_z v_y} & \sigma_{v_z v_z} \end{bmatrix} \tag{2-5}$$

In Figure 2-2, a Gaussian blob which describes the covariance σ_{xv_x} between the two variables x and v_x is shown. You can think of the blob as a region of likelihood where a high color intensity stands for a high probability, while a low color intensity stands for a low probability. In Figure 2-2 it can be seen, that an increase in variable v_x usually goes within an increase in variable x. This is what we would also expect. A positive change in velocity in a certain direction will also result in a positive change of position in the same direction.

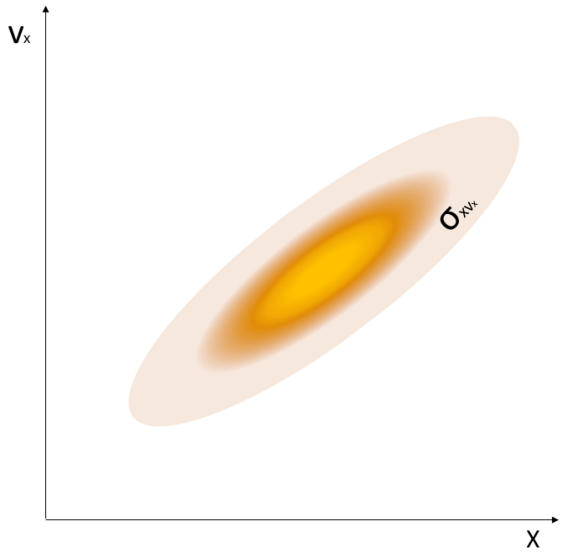

Figure 2-2: Joint variability of two variables. In this case the position and velocity in x direction

Accuracies of the measured state $\mathbf{R}$ as well as the uncertainties in the predicted state $\mathbf{P}_p$ are both defined using covariance matrices. Similar as the prediction derived from the previous state, the uncertainty in the prediction is derived using the uncertainty of the previous state $\mathbf{P}_{s_t}$ as well as the term $\mathbf{B}\vec{Q}\mathbf{B}^\top$

$$\mathbf{P}_{p_{t+dt}} = \mathbf{F}\mathbf{P}_{s_t}\mathbf{F}^\top + \mathbf{B}\vec{Q}\mathbf{B}^\top \tag{2-6}$$

While $\vec{Q}$ consists of accelerations which are describing the uncertainties of the environment like e.g. currents, $\mathbf{B}$ is a conversion matrix with information on the timestep. For our navigation problem, $\mathbf{B}$ and $\vec{Q}$ would have the following shape:

$$\mathbf{B} = \begin{bmatrix} \frac{dt^2}{2} & 0 & 0 \\ 0 & \frac{dt^2}{2} & 0 \\ 0 & 0 & \frac{dt^2}{2} \\ dt & 0 & 0 \\ 0 & dt & 0 \\ 0 & 0 & dt \end{bmatrix} \tag{2-7}$$

$$\vec{Q} = \begin{bmatrix} a_x^2 \\ a_y^2 \\ a_z^2 \end{bmatrix} \tag{2-8}$$

The values for a_x, a_y, a_z are hereby the maximum accelerations caused by the local environment that we would expect.

2-2-3 Kalman gain

Knowing the uncertainty of the predicted state $\mathbf{P}_p$ as well as the accuracy of the measured state $\mathbf{R}$, we can now weigh on the prediction and measurements in order to determine the new state with its uncertainty. Therefore we first construct a weighting matrix based on the prediction uncertainties $\mathbf{P}_p$ and the measurement accuracies $\mathbf{R}$:

$$\mathbf{K} = \frac{\mathbf{P}_p}{\mathbf{P}_p + \mathbf{R}} \tag{2-9}$$

This weighting matrix $\mathbf{K}$ is called the Kalman gain and can be used to update the state $\vec{x}_{s_{t+dt}}$ as well as the state uncertainties $\mathbf{P}_s$ as seen in Figure 2-4:

$$\vec{x}_{s_{t+dt}} = \vec{x}_p + \mathbf{K}(\vec{z} - \vec{x}_p) \tag{2-10}$$

$$\mathbf{P}_s = \mathbf{P}_p - \mathbf{K}\mathbf{P}_p \tag{2-11}$$

It can be seen, that if a value of the measurement covariance matrix of $\mathbf{R}$ is very large

compared to the value of the prediction covariance matrix $\mathbf{P}_p$, the corresponding term in the Kalman gain will converge to zero which means the algorithm honors the prediction instead of the measurement. On the other hand, having a large uncertainty in the prediction compared to to the accuracy of the measurement will lead to a Kalman gain close to one, which will result in honoring the values of the measurement $\vec{z}$ instead of the prediction $\vec{x}_p$. This is shown in Figure 2-3 and Figure 2-4. The new state $\vec{x}_{s_{t+dt}}$ with its uncertainty $\mathbf{P}_s$, shown in green is calculated based on the prediction $\vec{x}_{p_{t+dt}}$ and the prediction uncertainty $\mathbf{P}_p$ shown as a blue Gaussian blob, as well as the measurement $\vec{z}_{t+dt}$ and the accuracy in the measurement $\mathbf{R}$ shown as the yellow blob.

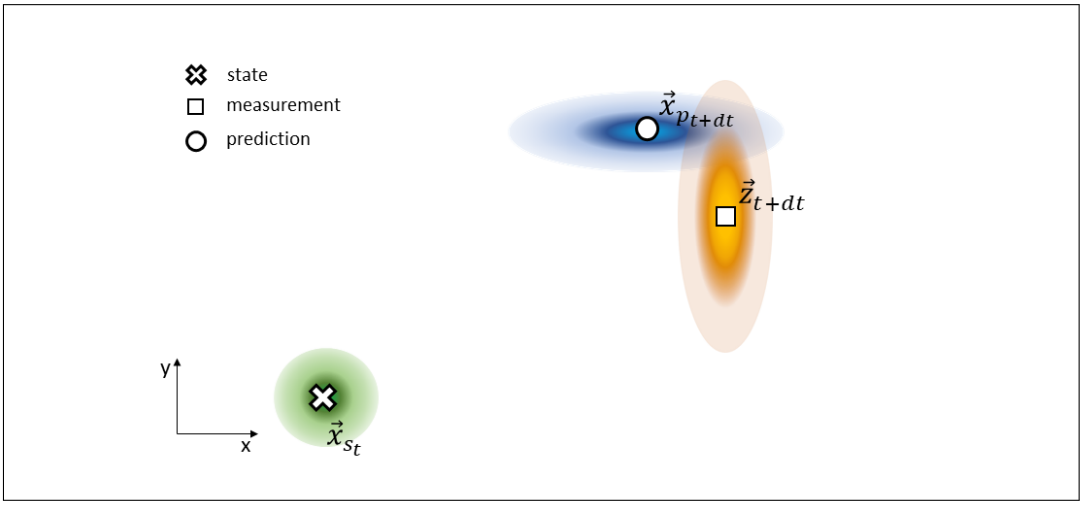

Figure 2-3: Prediction uncertainty (blue), state uncertainty (green), measurement accuracy (yellow)

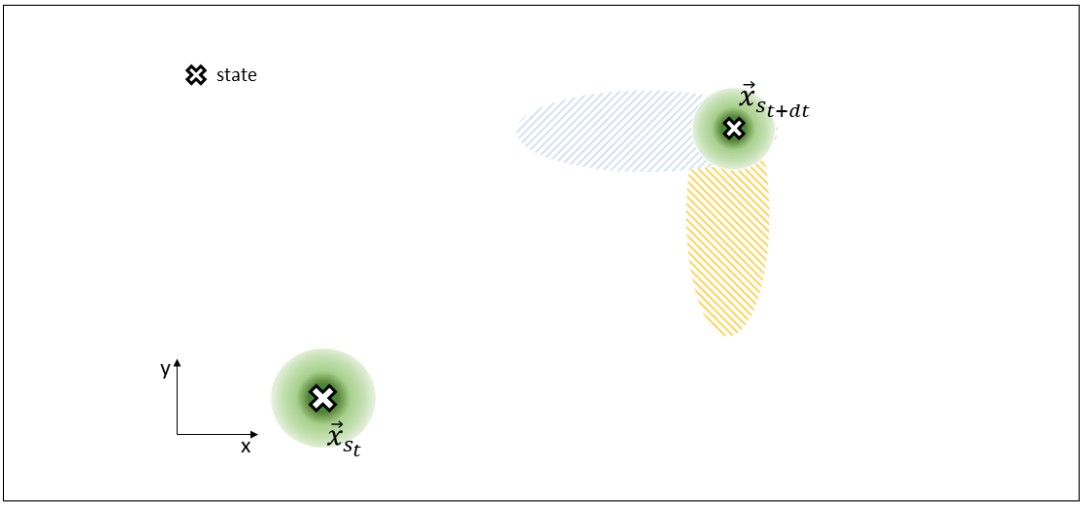

Figure 2-4: Updating state and state-uncertainty

2-3 Terrain based navigation (TBN)

We reintroduce measurement vector $\vec{z} = (x, y, z, v_x, v_y, v_z)^\top$. Thereby the operating water depth z is acquired by pressure sensors and the velocities v_x, v_y, v_z are acquired by the inertial navigation system (INS) of the vehicle.

In order to get the (x, y) coordinates of the AUV we make use of seabed topography data from existing bathymetry. This information about the sea bottom could come from the previously acquired seismic data which would have a very low lateral resolution in the crossline direction.

2-3-1 Low wave number approach to find x,y

The pre-existing data is assumed to be sparsely sampled with a spatial resolution of several 10ths of meters. This will lead to a low wave number topography (see dashed line in Figure 2-5) where the vehicle is navigated on. Of course, we would also expect topographic behaviour containing higher wave numbers (see solid line in Figure 2-5), which we set out to map correctly).

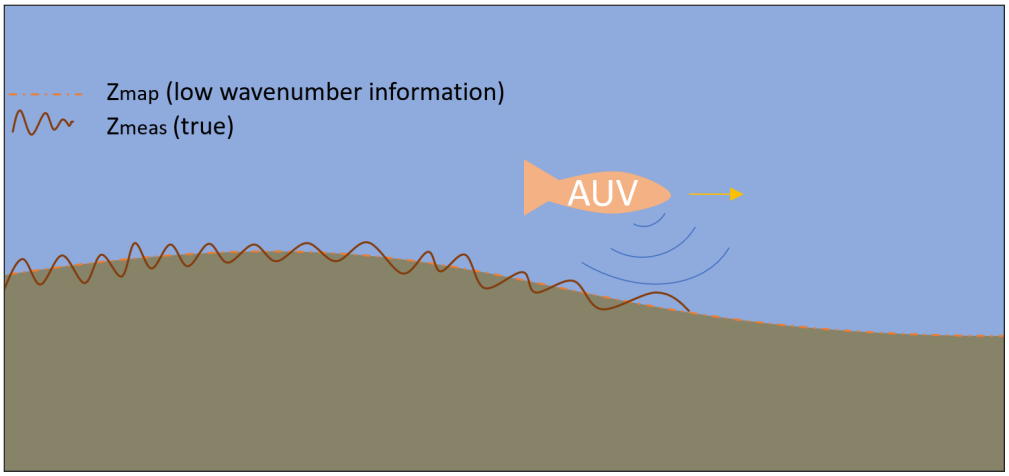

Figure 2-5: Low wave number approach

We assume that

1. the sparsely sampled data gives correct relations between water depths and coordinates,
2. the vehicle operates in constant height relative to the seabottom, and
3. the measurements coming form the AUV are taken perpendicular to the vehicle.

The depth levels of the interferometric side-scan measurements $\vec{Z}_{meas}$ (shown as the triangles on the orange line in Figure 2-6) are being compared to the topography of $\vec{Z}_{map}$ in the surrounding area of $\vec{x}_{p_{t+dt}}$. Therefore we set up the following objective function **J** which defines the difference between $\vec{Z}_{meas}$ and $\vec{Z}_{map}$ for points (x,y) in the area around the point (x_p, y_p).

$$\mathbf{J}(x,y) = \gamma[(x-x_p)^2 + (y-y_p)^2] + \sum_i [\vec{Z}_{map}(x,y,i) - \vec{Z}_{meas}(i)]^2 \tag{2-12}$$

We include a weighting factor γ which acts on the distance between the (x, y) point and the point (x_p, y_p) (green point in Figure 2-6). This is done to let the algorithm should honor values rather close to the prediction if similar depth differences are present.

The x and y values where $\mathbf{J}$ is minimal are now being extracted and set as the new positional values in measurement vector $\vec{z}$ (yellow point on Figure 2-6).

It has to be noted that the point to be substituted is not correct due to the previous explained high wave number deviations between $\vec{Z}_{meas}$ and $\vec{Z}_{map}$. This is illustrated in Figure 2-6 where the yellow dot does not exactly positional itself on top of the true position represented by the orange dot. However this high wave number effect will average out over multiple measurements in the Kalman filter.

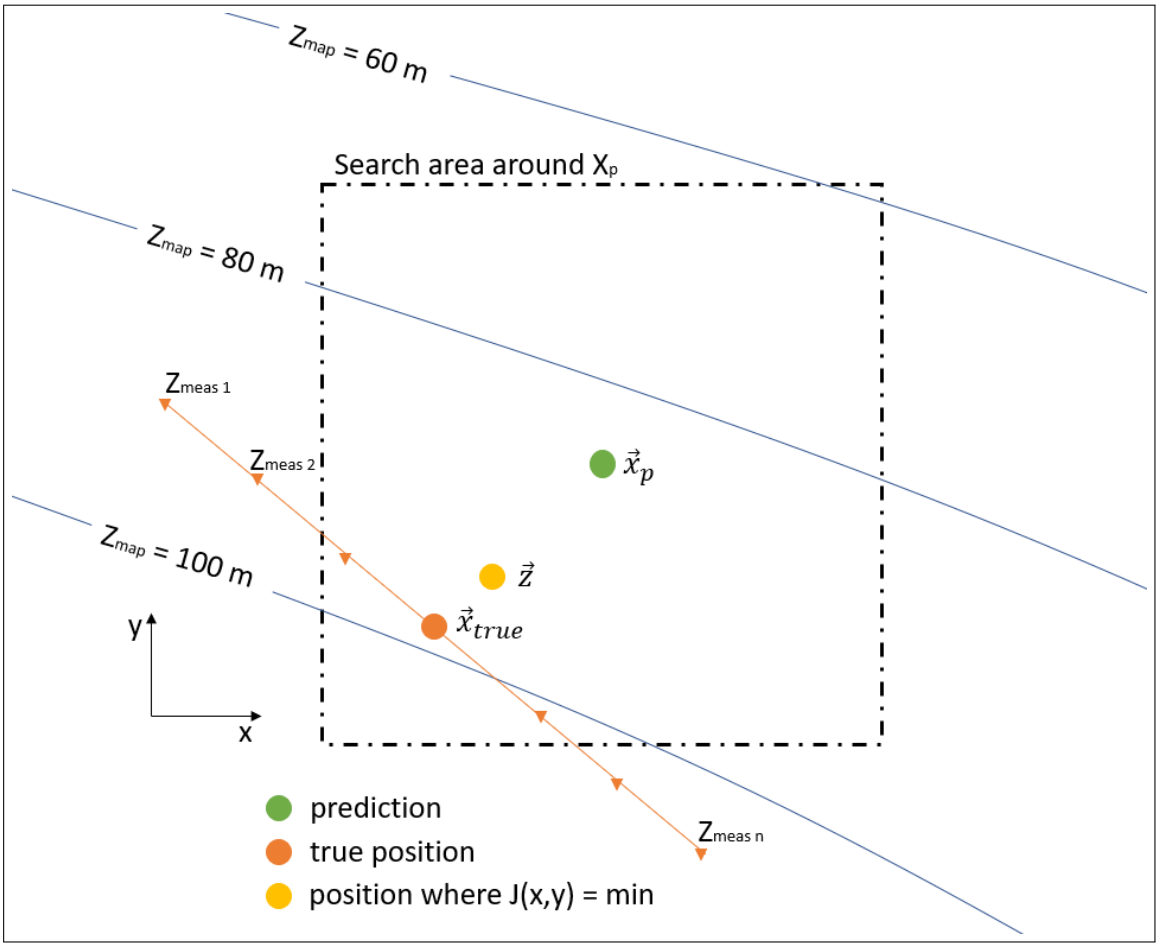

Figure 2-6: Terrain based navigation scheme

2-3-2 Quantifying measurement accuracies in TBN

Since the main part of the Kalman filter is to quantify uncertainties, the following approach was used to quantify the spatial variances and covariances of matrix $\mathbf{R}$ acting on the (x, y) estimates of measurement vector $\vec{z}$.

If positional information would be be acquired by GPS, the uncertainties would be of static nature and strongly depend on the accuracy of the device itself as well as its calibration. Since comparability between measured depth and the available sea bottom data is highly dependent on the topography of the seafloor we propose a dynamic change of accuracy which we set to be inversely dependent on the gradient of the bathymetry.

If the gradient is not parallel to the (x, y) axis (illustrated in Figure 2-7), it will lead to dependencies between the spacial variables and the covariances σ_{xy} and σ_{yx} will be non zero. Therefore a coordinate transformation is applied.

The variances along the (a, b) axes of Figure 2-7 are:

$$\mathbf{R}_{ab} = \begin{bmatrix} \sigma_{aa} & 0 \\ 0 & \sigma_{bb} \end{bmatrix} \tag{2-13}$$

Hereby σ_{aa} is the variance in the direction of the steepest descent and σ_{bb} the variance of the direction perpendicular to the steepest descent. We define these variances as follows:

$$\sigma_{aa} = \frac{\alpha^2}{||\frac{\partial Z}{\partial y} + \frac{\partial Z}{\partial x}||} \qquad \sigma_{bb} = \frac{\alpha^2}{||\frac{\partial Z}{\partial y} - \frac{\partial Z}{\partial x}||} \tag{2-14}$$

We can now back transform the values contained in $\mathbf{R}_{ab}$ into the spatial variances and co-variances related to the original orientation of x and y contained in matrix $\mathbf{R}$. For this we define the conversion matrix $\mathbf{M}$ with β being the direction of the steepest descent:

$$\mathbf{M} = \begin{bmatrix} sin\beta & cos\beta \\ cos\beta & -sin\beta \end{bmatrix} \tag{2-15}$$

Applying the following matrix multiplication finally leads to the $\mathbf{R}_{xy}$ values which can than be substituted back into the measurement accuracy matrix $\mathbf{R}$:

$$\mathbf{R}_{xy} = \mathbf{M}\mathbf{R}_{ab}\mathbf{M}^\top \tag{2-16}$$

$\mathbf{R}_{xy}$ can now be substituted into the spacial variance and co-variance parts of $\mathbf{R}$ which is than used to calculate the Kalman gain $\mathbf{K}$ after equation 2-9. The updated Kalman gain can now be used together with the measurement vector $\vec{z}$ containing the substituted positional values to estimate the new state $\vec{x}_{s_{t+dt}}$.

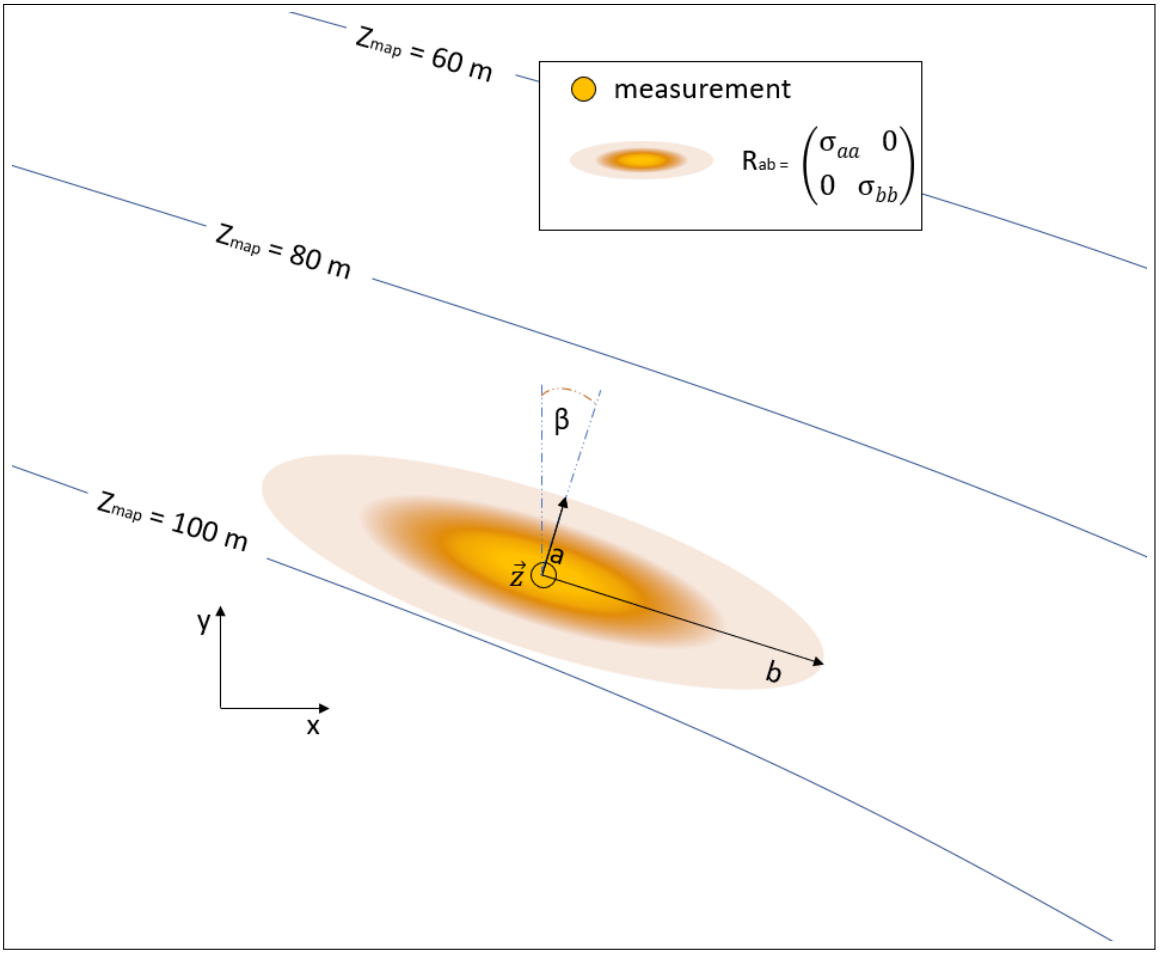

Figure 2-7: Terrain dependent uncertainties: the uncertainty increases if gradient is small

2-4 Model set up

In Figure 2-8 the low wave number sea bottom model can be seen with the true path of the AUV covering the area. The starting point of 50 m in x direction and 50 m in y direction was chosen. The seabottom has a wavelength of 150 m in the y direction and a slope in the x direction which could represent a shelf with a steepness of 10%.

In order to test the algorithms efficiency, an error to the velocity measurements of the INS is introduced which is set to be randomly distributed between 0 m/s and 0.2 m/s. This velocity error will result in a growing positional error between estimated state and true position and therefore the TBN is used in order to restrict this effect from happening. The algorithm recognizes the fact that $\vec{Z}_{meas}$ is not similar to $\vec{Z}_{map}$. It will set the positional values in the measurement vector closer to the true position and prevent a drastic increase of the error between the true and the estimated position.

To test the robustness of the algorithm, different high wave number components with different amplitudes where added to the topography. A wavelength of 40 m was added with amplitudes of magnitude 1 m and 3 m.

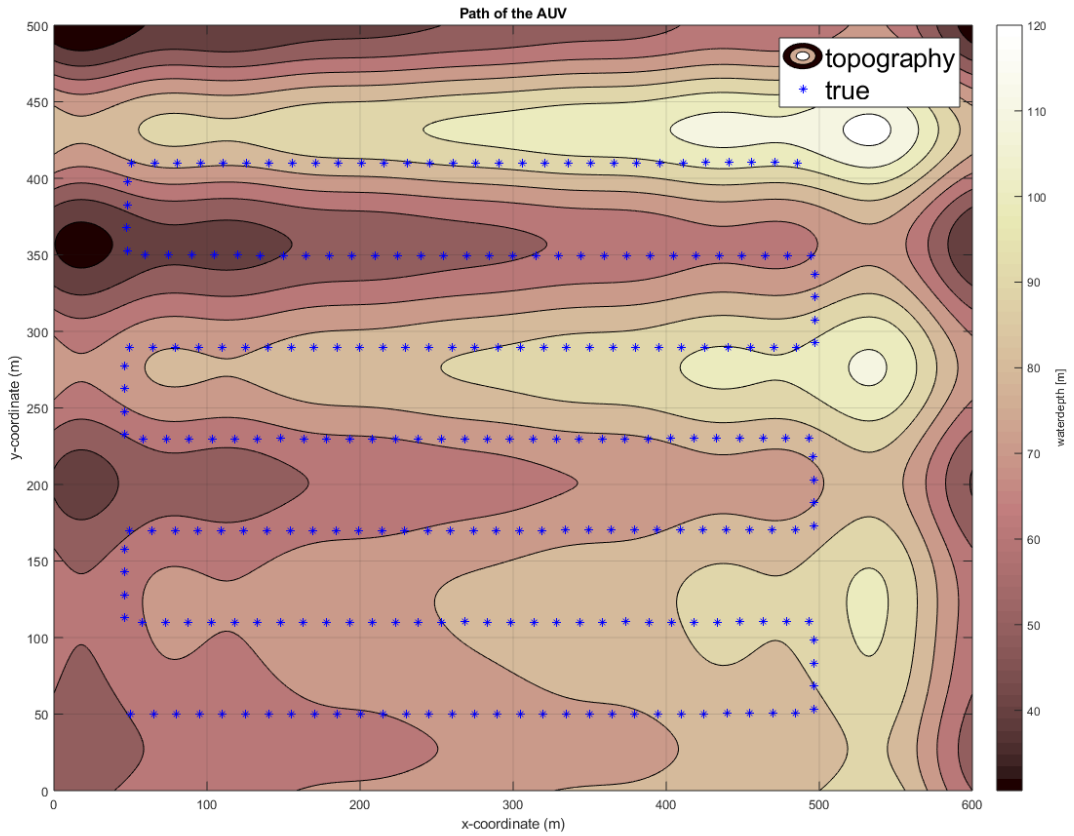

Figure 2-8: Low wave number model of sea bottom with true path of AUV used for all simulations

For running the simulation, the parameters in table 2-1 were chosen:

Description	Parameter	Value
number of time steps	nt	1170
time sampling	dt	1 s
initial x-position	x_0	50 m
initial y-value	y_0	50 m
true initial x-position	$x_{0_{true}}$	50 m
true initial y-value	$y_{0_{true}}$	50 m
initial velocity	v_0	3 m/s
maximum x acceleration	a_x	0.16 m/s^2
maximum y acceleration	a_y	0.16 m/s^2

Table 2-1: Table of Parameters.

We chose a weaved path to let the AUV cover the whole map, where the propagation direction of the vehicle is set to be parallel to the axes for simplicity reasons. Also we assume to have no vertical measurement errors and the vehicle operates with a constant height of 30 m over the sea bottom. Assuming a side-scan angle of 45°, a coverage of 30 m to each side of the vehicle is achieved. Therefore driving weaves with a separation of 50 m will give a sufficient overlap of 10 m, ensuring no void space in the data.

2-5 Results

We now show the results achieved using TBN. First (section 2-5-1) we compare a situation where we do not use seabottom information but just the information coming from the INS of the AUV, with the TBN approach. Secondly (section 2-5-2) different high wave number maps are tried out to test how stable the algorithm is for cases of big deviations between the measured and the apriori information. At last (section 2-5-3) the case was observed where a starting error between the first estimated position and the true position was introduced. In all the shown simulations every 10th iteration is visualized of a total number of 1170 measurements.

2-5-1 Comparison: INS only and TBN

The following results (Figure 2-9) were achieved using just the velocity data from the INS and the predicted values using the kinematic equations in the prediction matrix. It can clearly be seen that the positive INS error introduces the growing positional error between the true position and the estimated state. The vehicle is not able to prevent the error from growing.

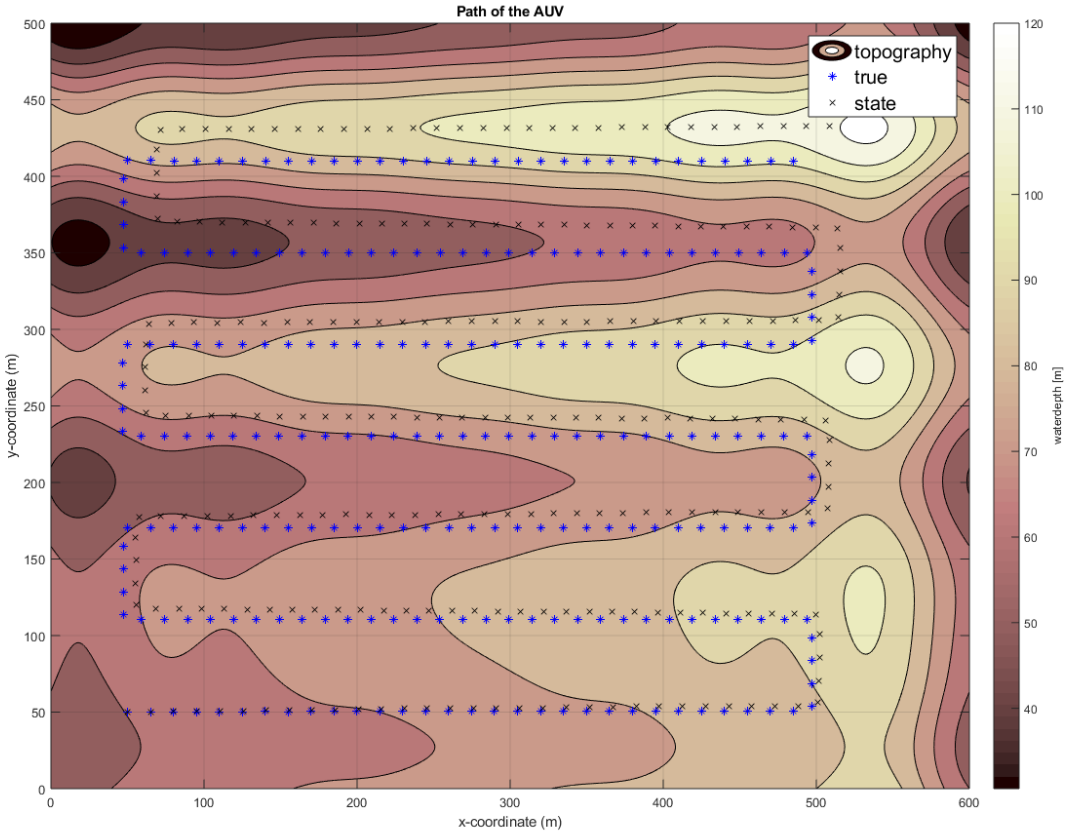

Figure 2-9: Navigation result: using INS data only is showing an increasing positional error

Now observing the result (Figure 2-10) using the proposed terrain based navigation approach, it is obvious that the positional error does not grow like in result (Figure 2-9). It can nearly perfectly orientate itself at the terrain data, preventing the INS velocity error to blend into a positional error.

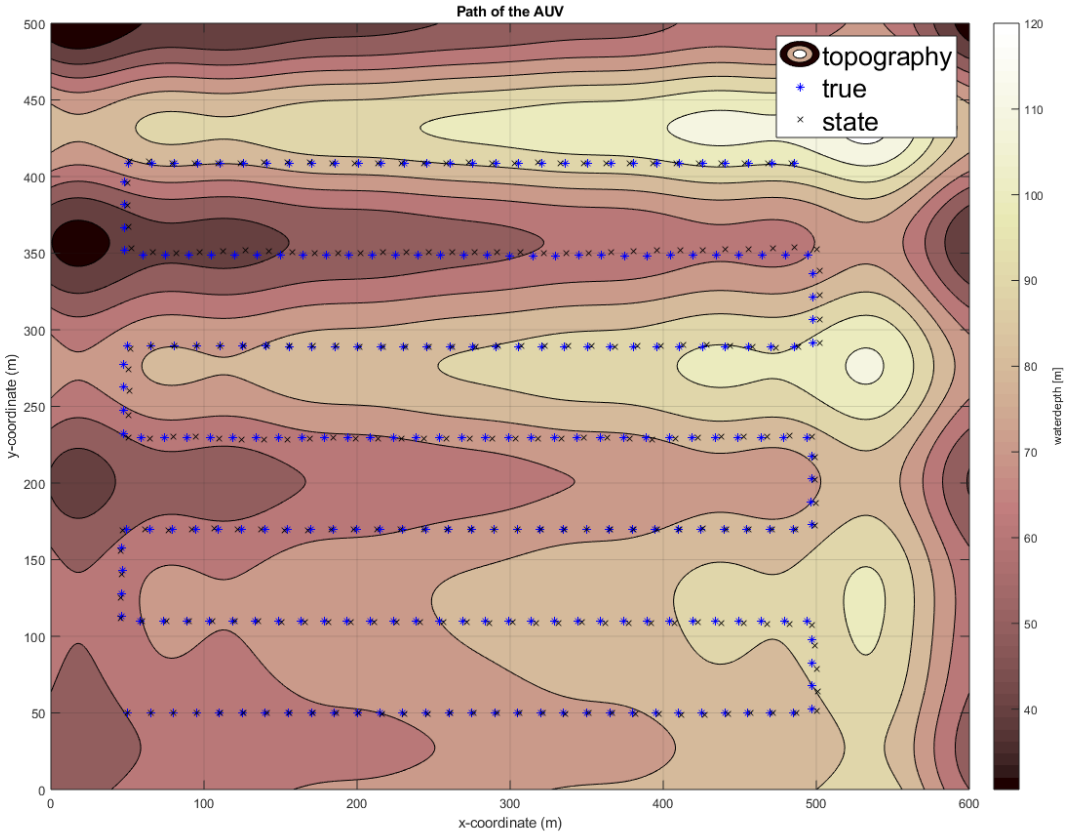

Figure 2-10: Navigation result: terrain based navigation: TBN prevents positional error from growing

2-5-2 High wave number results

Now a more realistic model is shown where the true model does differ from the sea bottom data used for the orientation. Looking at the result in Figure 2-11 where wavelengths of 40 m and amplitude of 1 m where added, it can be observed that the algorithm is still stable, and it still prevents a spread from the true position to a position which is far off.

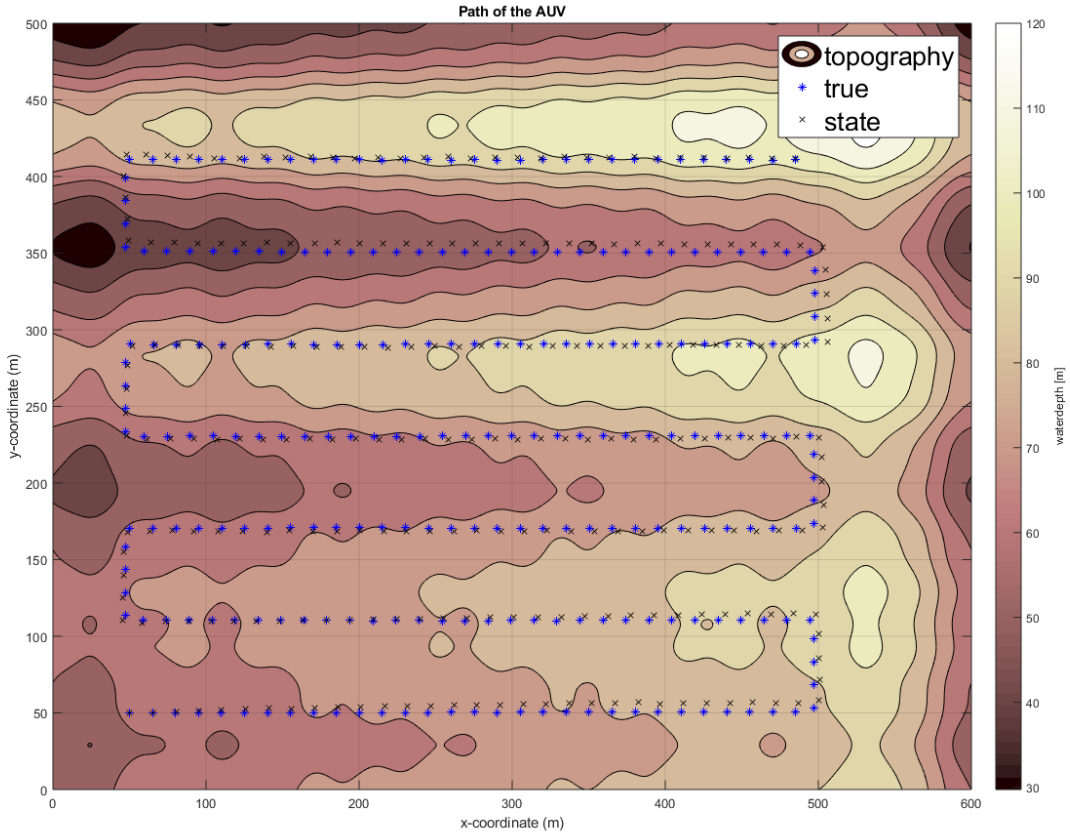

Figure 2-11: Navigation result: High wave number approach 1 m amplitude and 40 m wavelength

In the following Figure 2-12 the high wave number result is shown with inducing higher amplitudes of 3 m. It can be seen that the result is worse than with the 1 m amplitude where the topography doesn't differ too much from the expected map. At specific points, positional errors between estimated and true position of up to 10 m can be observed. However, 3 m amplitudes on 40 m wavelengths would mean slopes of more than 30% at most of the area which is far from realistic.

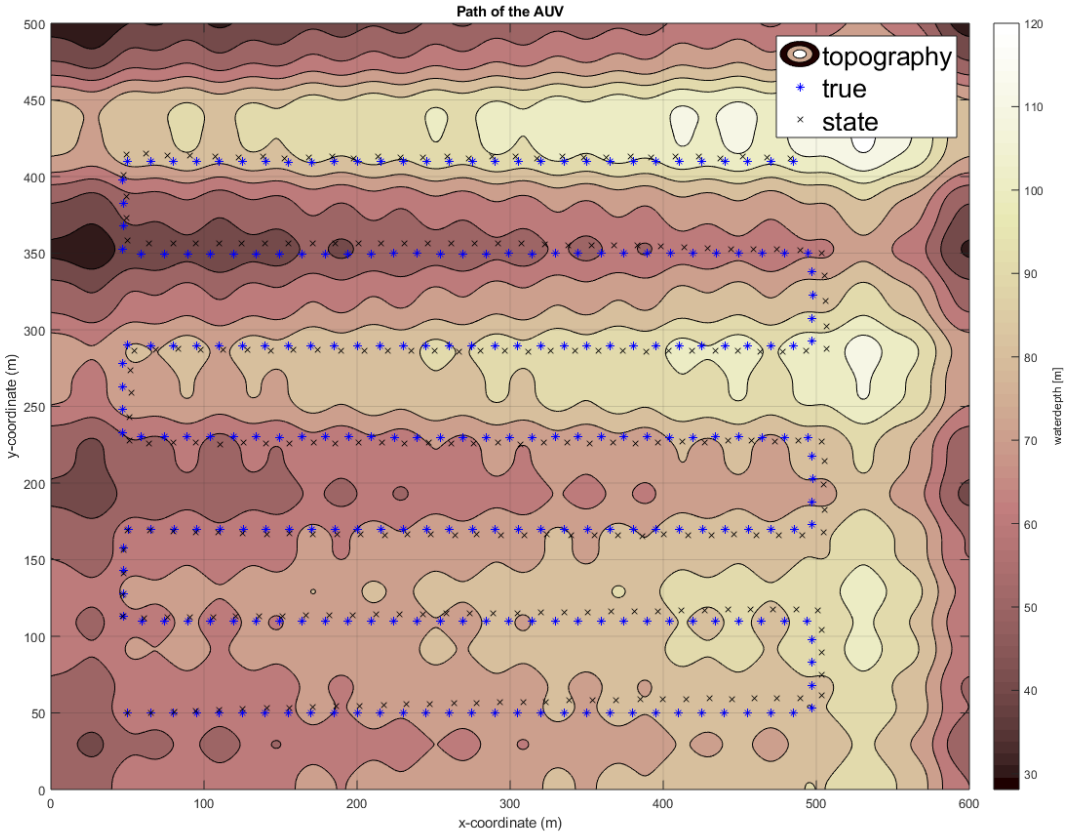

Figure 2-12: Navigation result: High wave number approach 3 m amplitude and 40 m wavelength showing increased errors compared to 1 m amplitude model

2-5-3 Starting error

Now we observe how the algorithm behaves if the first state is set to a wrong position. In a realistic scenario this will often be the case if the AUV transits from one measurement area to another measurement area. We still use the positive INS velocity error.

To show how the results would look like, not using topography data, we show the results only using the INS data. This is shown in Figure 2-13.

It can be seen, that the AUV is unable to correct its position to the point where the measured depth is also the true depth. Furthermore, we can see the same behaviour observed in section 2-5-1. With time the INS velocity error will induce a growing positional error. Running the simulation using TBN gives the result shown in Figure 2-14. It is clearly visible, that from the beginning, the assumed position of the state converges against the true position.

In the following Figure 2-15 the result is shown where we combine the high wave number approach with a false starting positioning. Also in this case, the AUV can successfully minimize the error between estimated and true position.

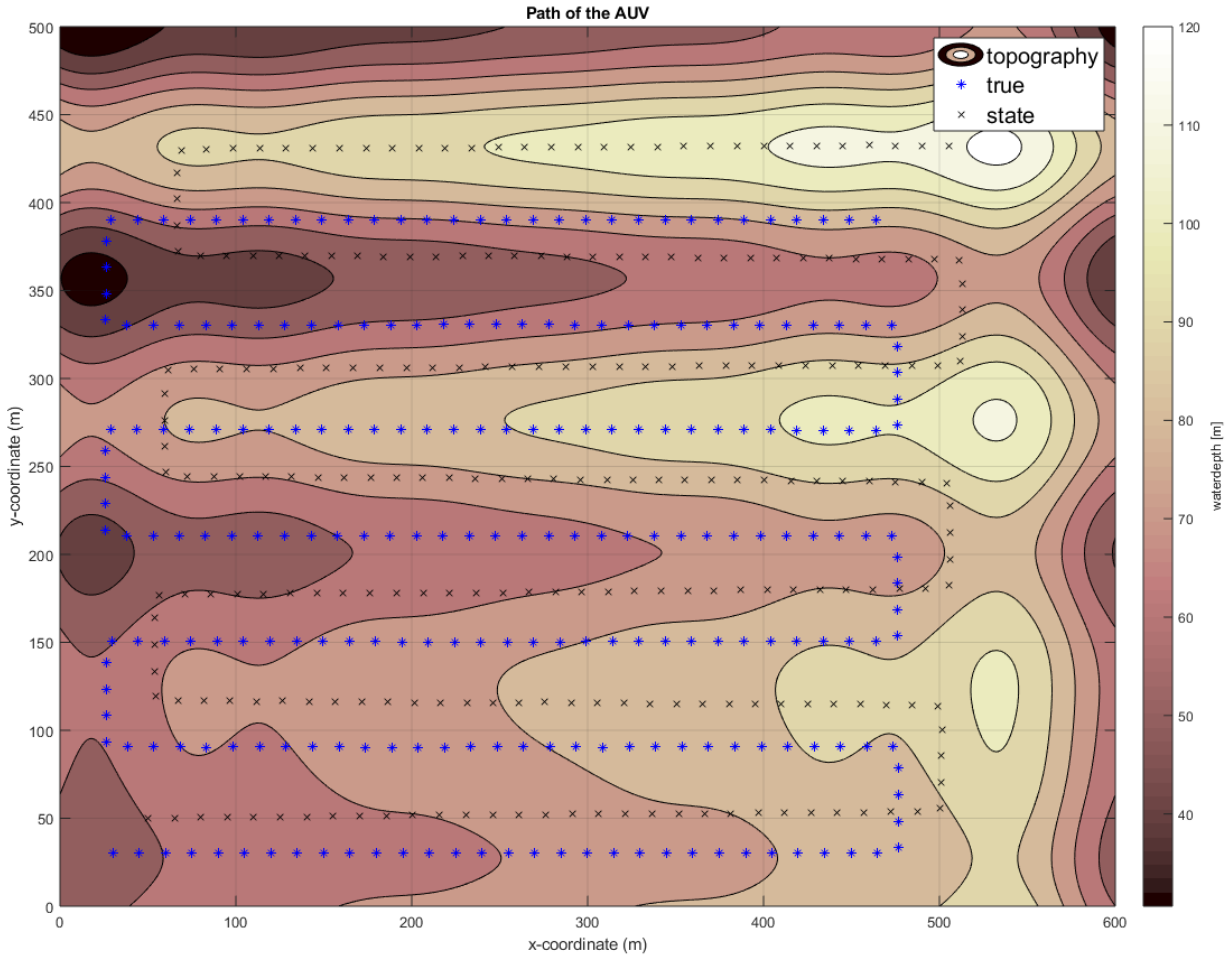

Figure 2-13: Navigation result including starting error: INS only is not able to find out true position

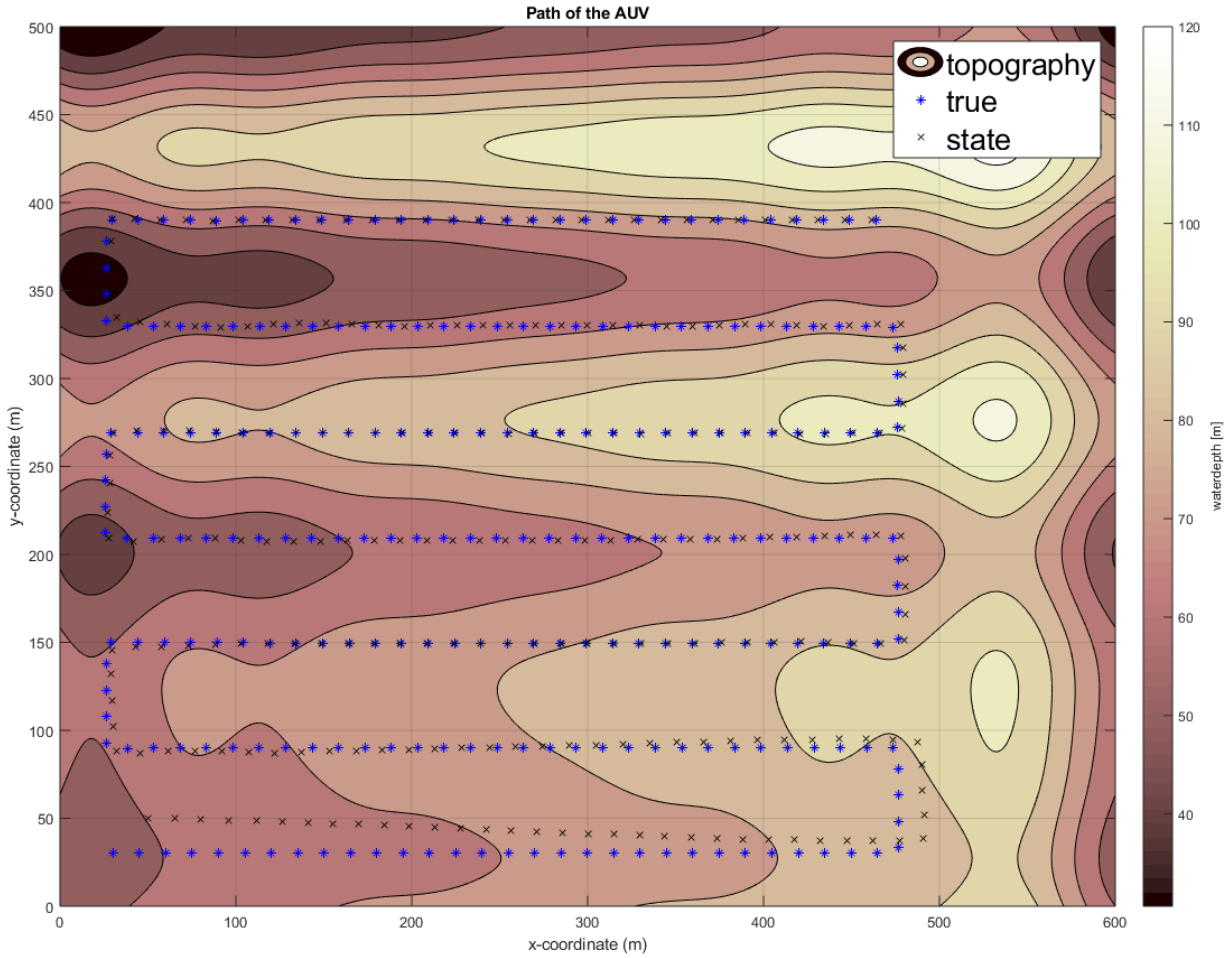

Figure 2-14: Navigation result including stating error: TBN showing ability to find out true position of vehicle

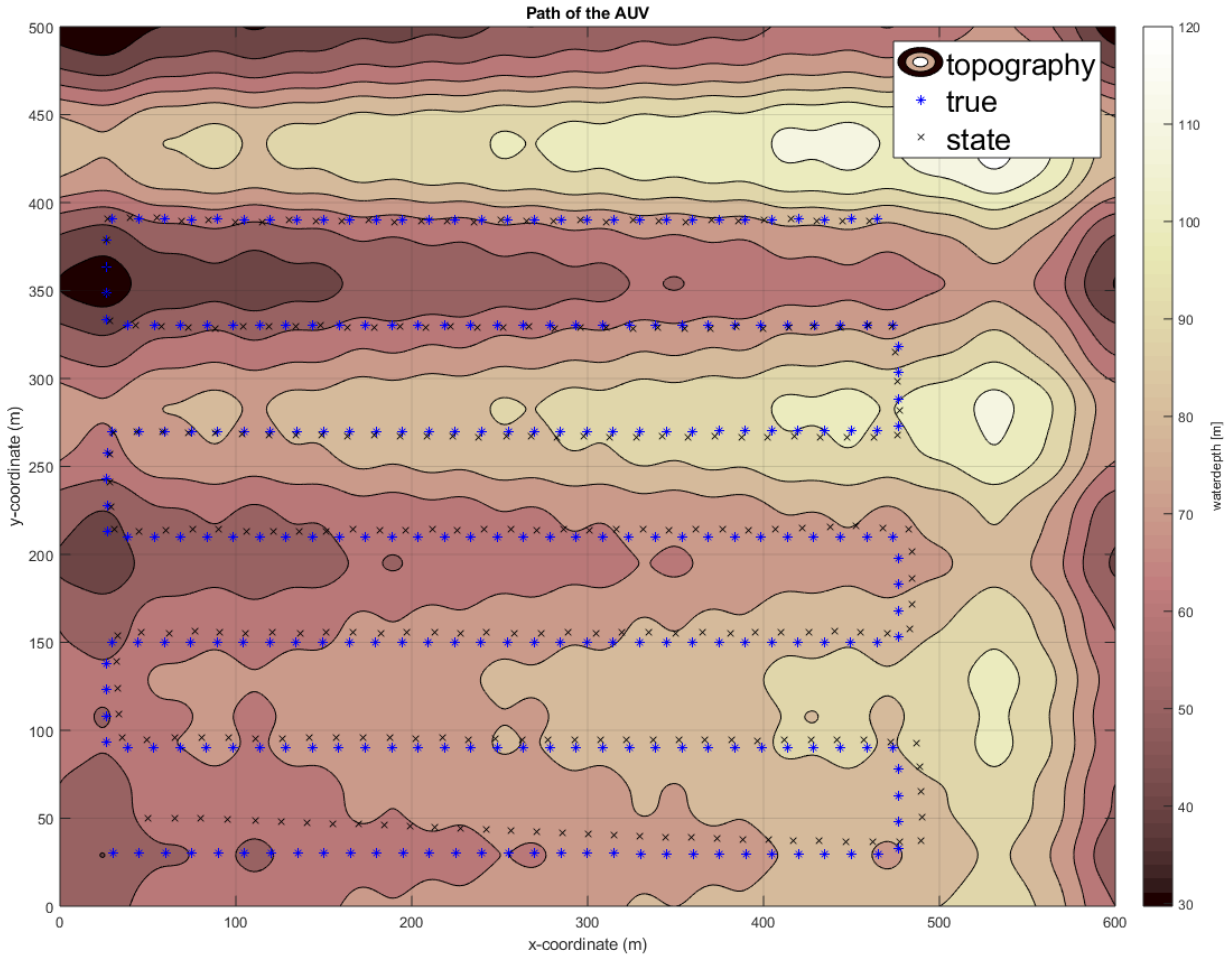

Figure 2-15: Naviagtion result including starting error: high wave number model (ISSS-TBN) showing ability to find out true position of vehicle

2-6 Conclusion

It was demonstrated, that the by an AUV recorded sea bottom during a mapping task can be a valuable source of information to improve the positioning of the AUV. By neglecting the x and y information obtained from depth information, the AUV is unable to correct its position. If the position of the vehicle is not correct, it is impossible for the AUV to get to know its true position with just making use of the velocity information of the INS. Furthermore when there are systematic errors in the data coming from the INS it will induce an error between the actual position and the estimated one. This can be prevented using the proposed terrain based navigation approach based on the Kalman filter. Furthermore it could be shown that high wave number fluctuations which differ from the used low wave number information does influence the positioning in a negative way if the added fluctuations have high amplitudes. However, one has to go to unrealistic scenarios (30% slopes) to get deviations larger than 10 m.

2-7 Discussion

The results of *Chapter 2* showed clearly that correction regarding position during bathymetric mapping tasks could successfully be improved.

Nevertheless this method can only be applied if data about the sea bottom topography is available and of sufficient quality, if this is not the case the method cannot be applied. In this case a SLAM like approach [Hammond and Rock, 2014] would be recommended where the AUV detects characteristic points of the seafloor which it aims to recognize again and subsequently rearranges the measured points. But also this method has its limitations as it assumes to have recognizable characteristic objects in the water which doesn't have to be the case in reality. This makes it also prone to errors if the setting is not the right one. Therefore we can always recommended to perform an evaluation regarding the topography and available data, before choosing the navigation approach.

Chapter 3

Full Wavefield Migration

3-1 Introduction

In *Chapter 3* we are going to observe how seismic imaging can be improved by incorporating multiples into the imaging process. Therefore an imaging algorithm is deployed which uses not just primary reflections but also multiple reflections to create images of the subsurface. First a brief introduction into seismic imaging (section 3-1-1) and multiple reflections (section 3-1-2) is being given, followed by an explanation of the imaging algorithm(section 3-2). Afterwards the approach (section 3-3) is being explained with which the imaging improvement was achieved (section 3-4).

3-1-1 Seismic imaging

Seismic imaging is used to create interpretable images of the subsurface for various applications from oil and gas exploration to CO_2 storage in the subsurface. In marine settings the conventional way is to acquire data from a ship through injecting acoustic waves into the subsurface by airguns. The wavefield gets reflected at boundaries of different material properties in the subsurface and travels up to the surface, where it can be recorded by arrays of hydrophones. This measured data, does of course not represent the true geometric relations of the geology and has to be processed. Seismic depth imaging aims to create an image from the recorded data, which can be interpreted structurally in terms of lithology as well as quantitatively in terms of elastic properties.

During conventional imaging, we make use of back-propagation of receiver wavefields, forward modeling of source wavefield and subsequently applying an imaging condition [Claerbout, 1971]. This imaging condition is most commonly a spatial cross correlation between receiver and source wavefield at every step in time. Furthermore another class of imaging algorithms has to be mentioned called inversion based imaging, where the acoustic response acquired in the field is being simulated by a model which is aimed to represent the true relations of reflectivity in the earth.

3-1-2 Multiples

In conventional seismic migration all signal is considered to come from primary reflections. Primary reflections are signals which reflected just once in the subsurface and getting transmitted back to the surface. However, the acquired data contains a lot of energy that reflected multiple times in the subsurface. These signals are called multiples. Particularly in marine seismic acquisition, multiples have a strong impact on the data since the water air interface leads to a nearly perfect reflection. Another important interface in creating multiples is the water sediment interface at the sea bottom. A lot of the energy gets reflected due to the big contrast in seismic velocity and density between sediments and seawater.

Multiple reflections can be classified as surface related multiples and internal multiples. While surface related multiples are reinjected into the earth at the surface, internal multiples experienced multiple scattering at interfaces below the surface level.

In conventional seismic imaging multiples are considered as coherent noise which have to be removed from the data. Recently, new methods have been developed to include multiples into the imaging process [Berkhout and Verschuur, 2011].

3-1-3 Sea bottom effect on seismic data

To observe how a wavefield in the subsurface is effected by a complex sea bottom topography we created two velocity models and let a wavefield from the surface propagate downwards by using a finite difference scheme. To simulate the air water contact a free surface boundary condition was implemented to create surface related multiples. We than recorded the downgoing wavefield below the sea bottom over a certain time interval. This was done in order to get an idea how the transmitted wavefield through the sea bottom with its surface related multiples will differ between flat (model B - Figure 3-1) and complex sea bottom (model A - Figure 3-1). The velocity models used to create the simulations are shown in Figure 3-1. Virtual receivers were then created at a depth level of 150 m. Since no reflectors are present under the sea bottom and an absorbing boundary condition was implemented on the lower boundary of the model, the wavefield that gets recorded at the receivers is solely of downgoing nature.

The created data is shown in Figure 3-2. It is clearly visible that a complex sea bottom will create complex wavefield propagation effects resulting in complex shaped wavefronts and diffractions (model A - Figure 3-2). This has to be accounted for in the imaging process, which is the objective of *Chapter 3* of this thesis.

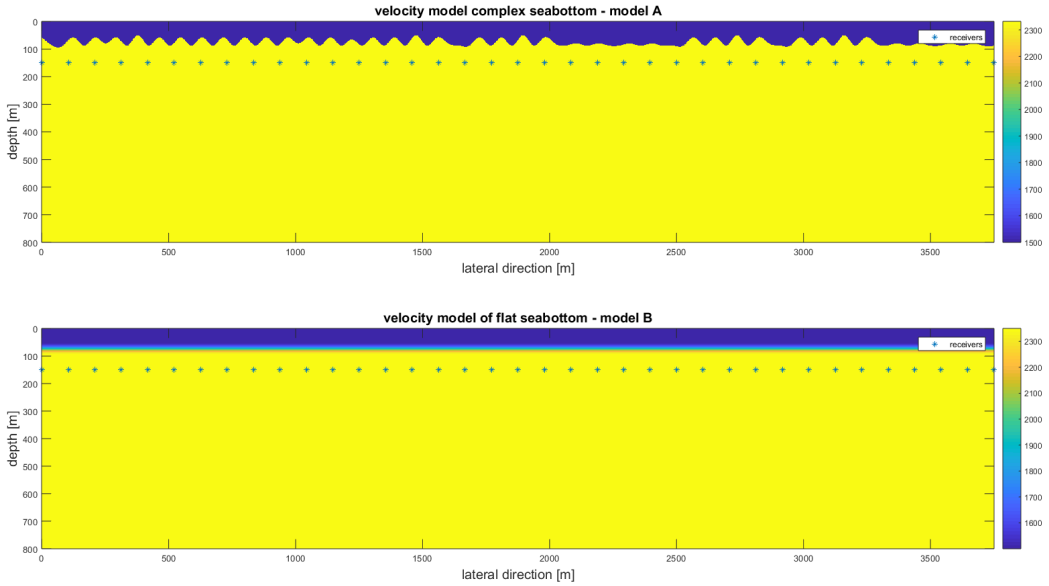

Figure 3-1: Velocity models to create downgoing wavefield under sea bottom

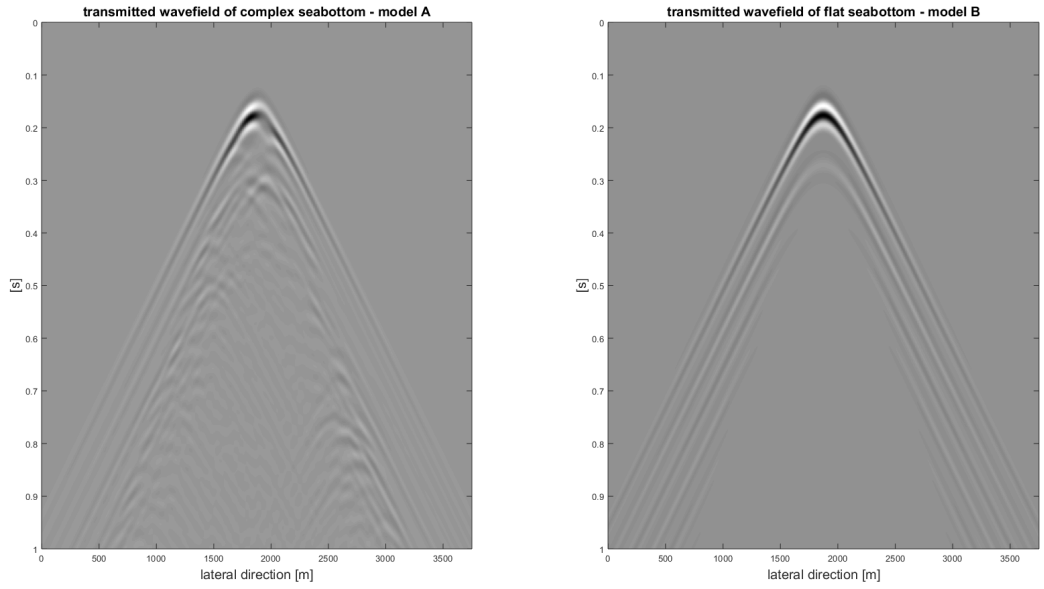

Figure 3-2: Comparison downgoing wavefield under sea bottom

3-2 Full wavefield migration

Full wavefield migration [Berkhout and Verschuur, 2011] is a depth imaging technique that makes use of multiple scattering effects in the subsurface. It uses an inversion based approach where measured data in the field is compared with a built model which should approximate the true model in depth, including all surface as well as internal multiples. It can be compared to full waveform inversion (FWI) [Tarantola, 1985]. However, where the inversion in FWI is done for seismic velocities in depth, full wavefield migration inverts for reflectivities in depth. The inversion in FWM is done by using one-way phase-shift operators based on a velocity model as well as reflectivity operators based on a model of reflection coefficients at each depth level. Each iteration of a propagation in the downward direction followed by a propagation in the upward direction will generate one additional order of scattering. Thereby an arbitrary amount of scattering can be introduced in the modeling process. During the modeling a smooth velocity model can be used. Different to reverse time migration [Baysal and Sherwood, 1983], the velocity model in FWM will just describe propagation effects, and is not responsible for generating scattering effects, as these are described separately.

3-2-1 Full wavefield modeling

In the following section the modeling process being the kernel of the inversion is being explained.

We make use of the matrix notation after [Berkhout, 1982]. Outgoing wavefields are hereby defined as Q wavefields and incoming wavefields are described as P wavefields. Thereby the monochromatic component of a wavefield can be described as a scalar, $P_{jk}(z_m, z_n)$ where j is defining the current grid point and k is defining the shot number. The depth level where the wavefield is observed is defined as z_n. The depth level where the wavefield got emitted is defined as z_m. One shot record can be described as $\vec{P}_k(z_m, z_n, \omega)$ and seismic data set containing multiple shots can be described as a matrix $\mathbf{P}(z_m, z_n, \omega)$

A superscript $+$ will hereby refer to the downgoing part of the wavefield while the superscript $-$ refers to the upgoing part of the wavefield. $\vec{Q}_m^+$ would than describe the outgoing downgoing wavefield at depth level m, which can be described as the superposition of the transmitted upgoing wavefield and the reflected downgoing wavefield. Similarly, $\vec{Q}_m^-$ would describe the outgoing upgoing wavefield at depth level m which would then consist of the transmitted upgoing and reflected downgoing wavefield at depth level m.

$$\begin{aligned}\vec{Q}^+(z_m) &= \mathbf{T}^+(z_m)\vec{P}^+(z_m) + \mathbf{R}^\cap(z_m)\vec{P}^-(z_m)\\ \vec{Q}^-(z_m) &= \mathbf{T}^-(z_m)\vec{P}^-(z_m) + \mathbf{R}^\cup(z_m)\vec{P}^+(z_m)\end{aligned} \tag{3-1}$$

The outgoing wavefields will than be transformed into incoming wavefields at the next depth level after the propagating operator $\mathbf{W}$ acts on the wavefield.

$$\begin{aligned}\vec{P}^-(z_{m-1}) &= \mathbf{W}^-(z_{m-1}, z_m)\vec{Q}^-(z_m)\\ \vec{P}^+(z_{m+1}) &= \mathbf{W}^+(z_{m+1}, z_m)\vec{Q}^+(z_m)\end{aligned} \tag{3-2}$$

At every depth level z_m, a reflectivity operator $\mathbf{R}(z_m)$ acts on the incident wavefield $\vec{P}$. Thereby the notation $\mathbf{R}^{\cap}(z_m)$ stands for the reflectivity acting on the upgoing incoming wavefield $\vec{P}_k^-(z_m)$, and $\mathbf{R}^{\cup}(z_m)$ the reflectivity acting on the downgoing incoming wavefield $\vec{P}_k^+(z_m)$. This is illustrated in Figure 3-3.

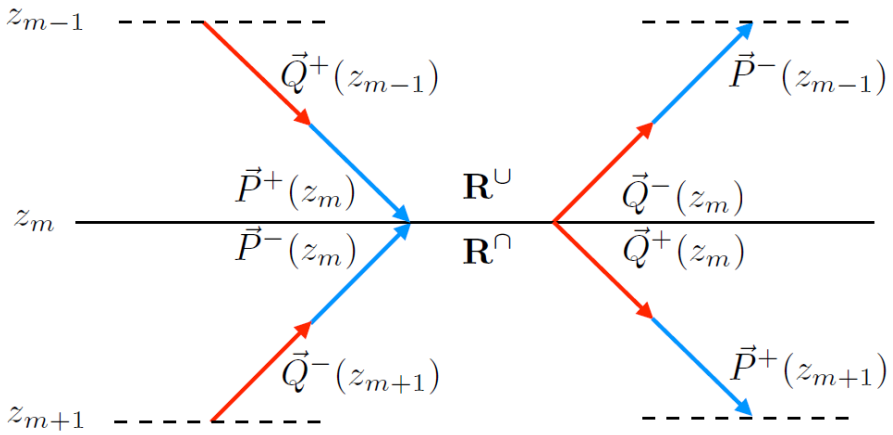

Figure 3-3: Forward modeling scheme used in the full wavefield migration scheme [Davydenko, 2016]

With these two sets of models we can simulate the upgoing wavefield with an arbitrary order of scattering included. This recursive wavefield modeling process is extensively described in [Berkhout, 2012].

3-2-2 Inversion

By making use of the described full wavefield modeling, a synthetic data set can now be generated which can then be compared to the measured data. This procedure is applied using a multi-frequency approach where first the lower frequency parts of the spectrum are inverted for and later on the higher frequencies are added until the inversion is completed for the full bandwidth of the data.

The minimization process can be described with the following cost function 3-3.

$$J(\mathbf{R}^{\cup}, \mathbf{R}^{\cap}) = \sum_{\omega} || \mathbf{P}^-_{meas}(z_0, z_0) - \mathbf{P}^-_{mod}(z_0, z_0) ||_2^2 \tag{3-3}$$

This cost function is being minimized in a conjugate-gradient scheme.

3-3 Approach

To test if sea bottom information has a positive effect on seismic imaging by full wavefield migration we create a synthetic data set.

Therefore a true model of reflectivity was created based on the velocity and density models (shown in Figures 3-4 and 3-5). The models were created containing several geological layers and some high velocity anomalies beneath the sea bottom. We introduce a free surface boundary at the top of the model by inducing a perfect reflector in the reflectivity model at z_0. This reflector should represent the water air interface at the sea surface. Thereby the downgoing wavefield at the surface can be described as:

$$\vec{Q}^{+}(z_0) = \vec{S}^{+}(z_0) + \mathbf{R}^{\cap}(z0)\vec{P}^{-}(z_0) \tag{3-4}$$

The outgoing downgoing wavefield $\vec{Q}^{+}(z_0)$ at the surface is represented by the injected source wavefield $\vec{S}^{+}$ and the reflected upgoing wavefield at the depth level of the surface z_0.

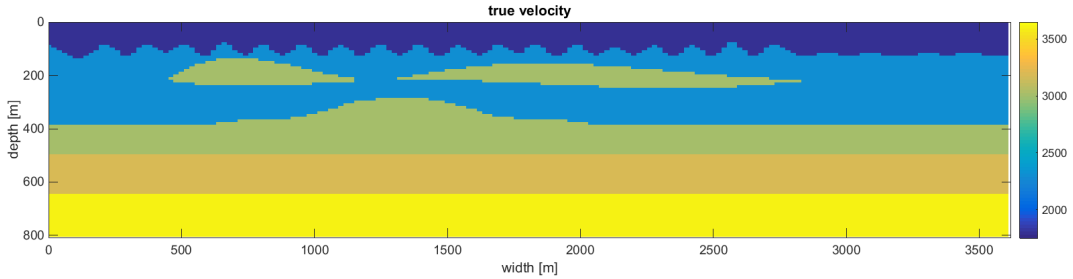

Figure 3-4: True velocity $[m/s]$ model used with the density model to create true reflectivity model

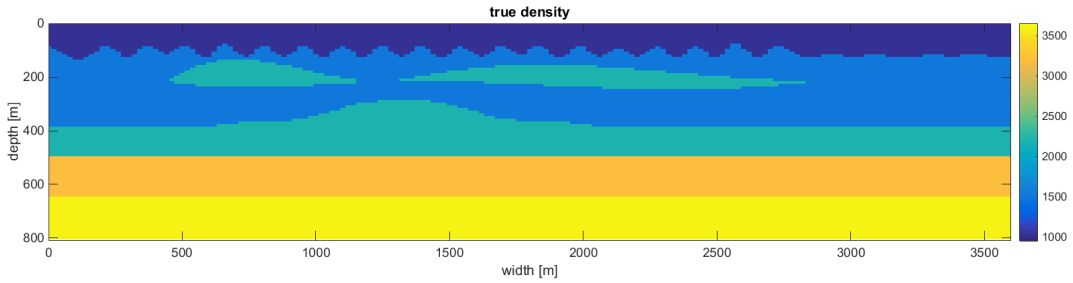

Figure 3-5: True density $[\frac{kg}{m^3}]$ model used with the velocity model to create true reflectivity model

Assuming normal incident conditions we can now calculate the reflectivities $\mathbf{R}$ depth which represents the true model we want to invert for. Thereby the reflection coefficient describes the portion of the energy that gets reflected at the interface from one to another medium and can be described as shown in equation 3-5:

$$R = \frac{\rho_1 v_1 - \rho_2 v_2}{\rho_1 v_1 + \rho_2 v_2} \tag{3-5}$$

Applying this condition for every depth level of our density and velocity models results in the following model of reflectivity $\mathbf{R}$ in depth 3-6.

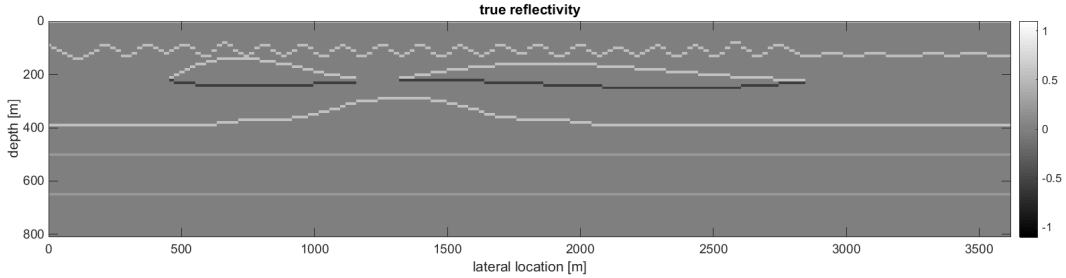

Figure 3-6: True reflectivity model used to create synthetic data

Making use of the velocity and reflectivity models combined with the full wavefield modeling algorithm, a synthetic data set $\mathbf{P}^{-}_{meas}(z_0, z_0)$ was created which we assume to be the measured data in the field. In the following Figure 3-7 a shot gather of a source position in the middle of the receiver line is shown. To create the shot gather a ricker wavelet was used with a dominant frequency of 25 Hz and a bandwith of 5 Hz to 40 Hz. The four frequency bands inverted for in the multi frequency approach where 5 Hz - 10 Hz, 5 Hz - 20 Hz, 5 Hz - 30 Hz, 5 Hz - 40 Hz.

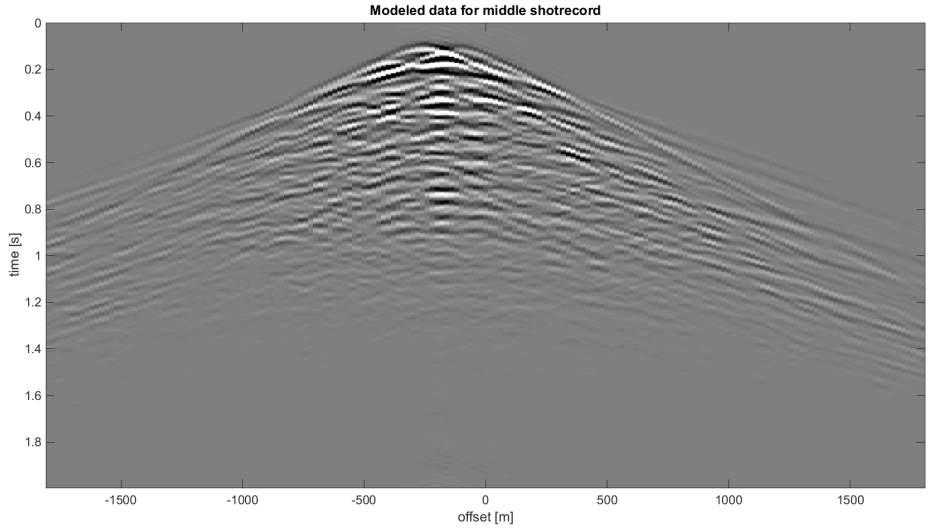

Figure 3-7: Shotrecord of synthetic data

Since inversion results are known to be highly uncertain, constraints can be added, based on apriori information from different data sources like well data. Therefore the initial models from which we start the inversion are an essential part in the inversions success. The approach taken in this work was to include a sharp version of the sea bottom into the smooth initial velocity model. Furthermore the reflection coefficient at the sea bottom is being calculated and included into the initial reflectivity model. We assume the impedance contrast between seawater and first layer is constant over the whole model.

In this work, for each acquisition setting, we ran two types of simulations.

3-3-1 Normal approach

In the normal approach the full wavefield migration was run with a smooth velocity model. As an initial reflectivity model, a blank model was chosen containing a perfect reflector on the surface simulating the water air interface at the sea surface.

In the the Figures 3-8 and 3-9 the initial models for running the inversions using the normal approach are shown:

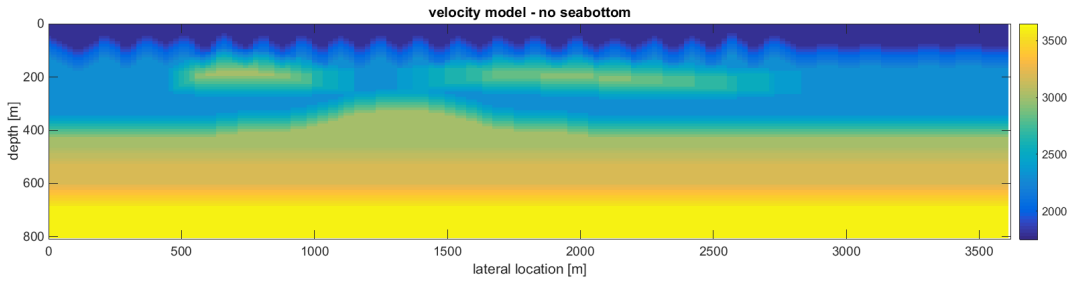

Figure 3-8: Initial velocity model for inversion not using sea bottom information

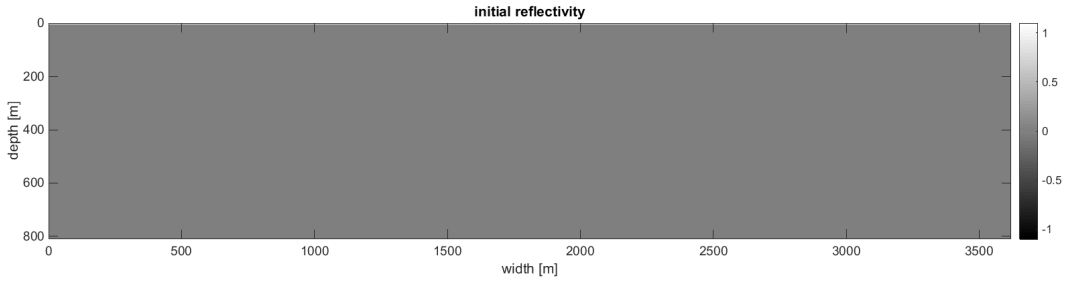

Figure 3-9: Initial reflectivity model for inversion not using sea bottom information

3-3-2 Sea bottom approach

To include the sea bottom into the full wavefield migration, the sea bottom topography was included into the initial models and the inversion was constrained to just update the area below the sea bottom. The sea bottom constrain was achieved by placing the exact sea bottom reflectivity into the estimated reflectivity model (Figure 3-11) after each iteration. Furthermore the upper part of the true velocity model, containing the sea bottom was substituted into the initial velocity model (Figure 3-10). This will result in a sharp velocity model in the area of the sea bottom. Below the sea bottom the velocity model is kept smooth as in the normal approach (section 3-3-1). Assuming the impedance contrast as well as topography contrast was assumed right, all the multiples created at this interface as well as the water sea bottom reflections can be described, and the updating will be focused on the events below.

The following initial models (Figures 3-10 and 3-11) were used to run the information making use of the sea bottom approach:

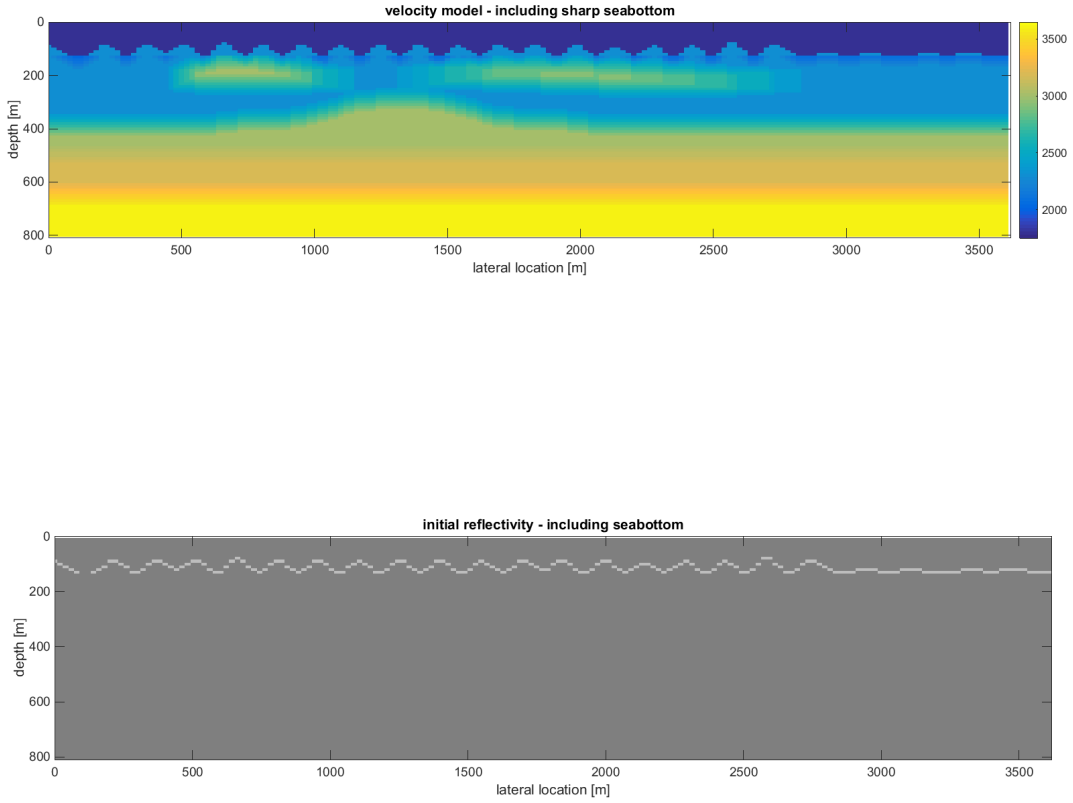

Figure 3-11: Initial reflectivity model used for inversion using sea bottom information

3-4 Results

3-4-1 Results with varying shot spacing

Figure 3-12 shows the inversion results at 20 m shot spacing. By looking at the result without including sea bottom information into the initial models we can see that the underlying structure could be represented correctly. The sea bottom could be imaged correctly but the image seems to be noisy in lower sections. Furthermore the part at a lateral location between 1500 m and 2000 m at a depth level of 400 m to 500 m is wrongly imaged after 22 iterations. This is due to the model that converged to a local minimum instead of the global minimum.

Comparing this result to the result obtained using the proposed sea bottom constraint, an improvement could be observed. It can clearly be seen that it has a positive effect on the signal to noise ratio. Furthermore the part at a lateral location between 1500 m and 2000 m at a depth level of 400 m to 500 m is being imaged correctly. Note that the part of the model including the sea bottom and the overlying grid cells didn't get updated in the inversion process and contains the true values of reflectivity.

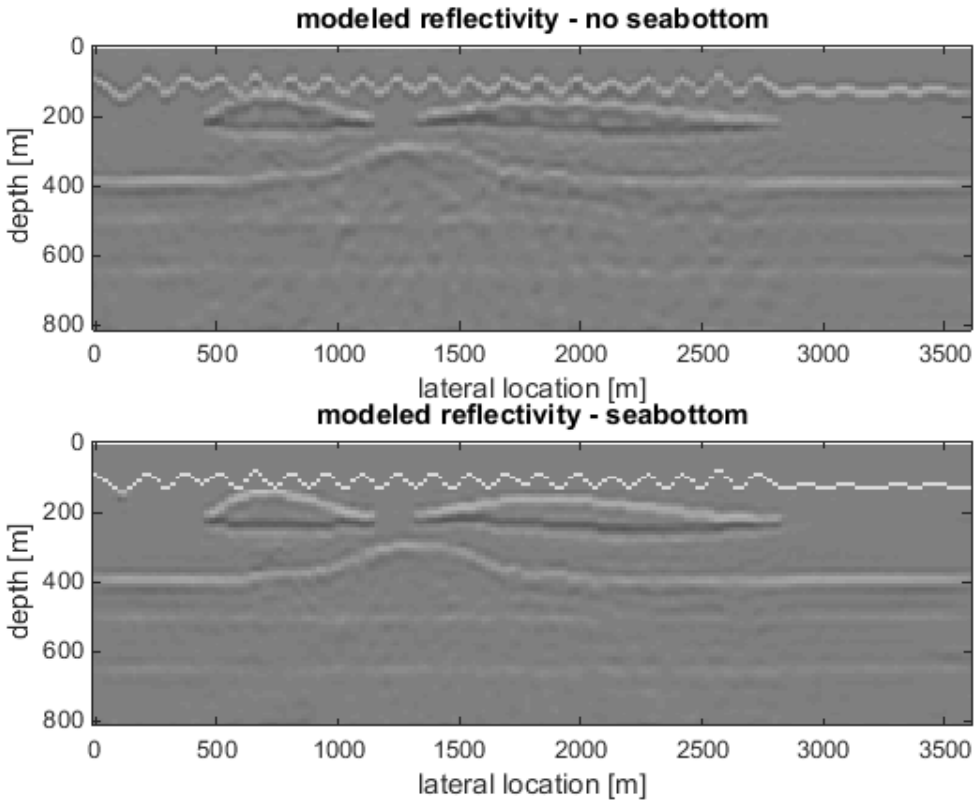

Figure 3-12: FWM comparison with sourcespacing of 20 m

Observing now the results for shot spacing of 100 m it can be seen, that the conditions of the image without the sea bottom constraint worsens significantly. The wrongly imaged structure from the simulations with smaller shot spacing is still not improved and even the first order sea bottom multiple is getting falsely imaged as a primary. It is also observable that in the area from 2500 m to 3600 m the inversion result represents the true reflectivity a lot better than in the area with complex sea bottom as well as complex geology in the area of 500 m to 2500 m. By looking at the result of the 100 m shot spacing with using the sea bottom constraint, it can be seen that the image didn't loose as much quality as the one with using a blank initial model. The reduction of image quality with increasing shot spacing seems not as intense with using sea bottom constraints.

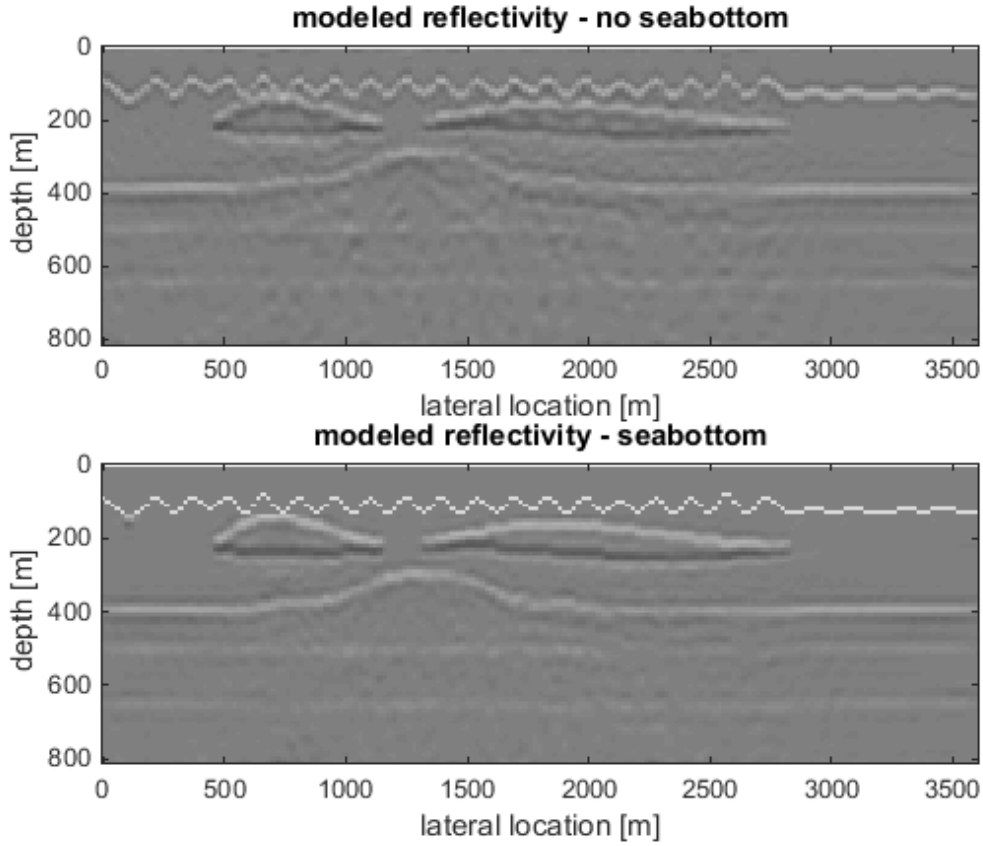

Figure 3-13: FWM comparison with source spacing of 100 m

We chose to run the simulation for shot a spacing of 400 m using 60 iterations. This is done in order to see if there will still be improvements after a very large amount of iterations. If this would be the case it would just show that constraining the inversion with the sea bottom would help the algorithm to get a quicker result, but not improve the image quality after all.

Looking at the results for a shot spacing of 400 m we can observe that the inversion gives an unreliable image. Neither the sea bottom is imaged correctly nor the sections at greater depths. Strong semi-spherical artifacts can be observed as well as overall blurriness. The blurriness of the image is the greatest in the area under the near surface anomaly. The inversion results in the section between 3000 m and 3600 m with flat sea bottom topography shows an acceptable image quality, but multiples are still falsely imaged as primaries. Observing the reflectivity image using the sea bottom constraint we can see that the image still represents the true model of reflectivity correctly. Even in the area of complex geology and complex sea bottom the image is clear and has a high signal to noise ratio.

The inversion result in Figure 3-14 is showing that even with a large amount of iterations, the image quality of the model without sea bottom constraint is still much worse than the one with the sea bottom constraint applied. Again semi-spherical artifacts around the near surface anomaly can be seen. Nevertheless a slight improvement in inverting for the sea bottom reflectivity can be observed. Especially in the area with complex geology, the signal to noise ratio appears to be much lower using no sea bottom information.

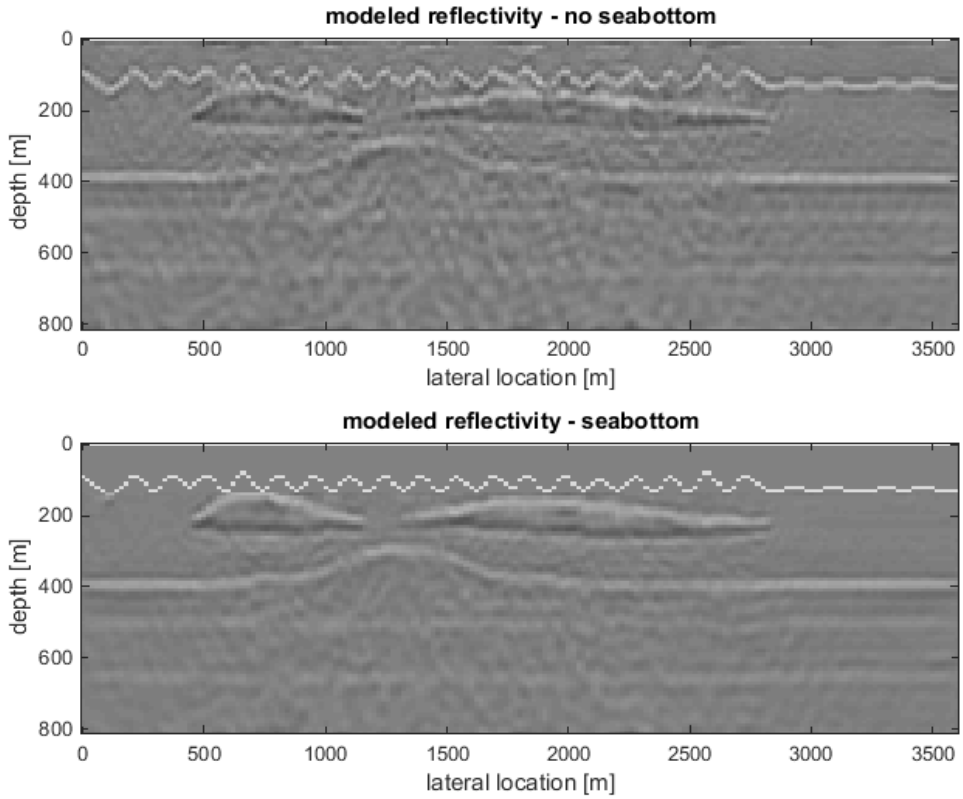

Figure 3-14: FWM comparison with source spacing of 400 m at 60 iterations

By observing the objective function (equation 3-3) of the inversions in Figure 3-17, it can be seen that the difference between total observed data and total measured data is lower during the inversion using the sea bottom information.

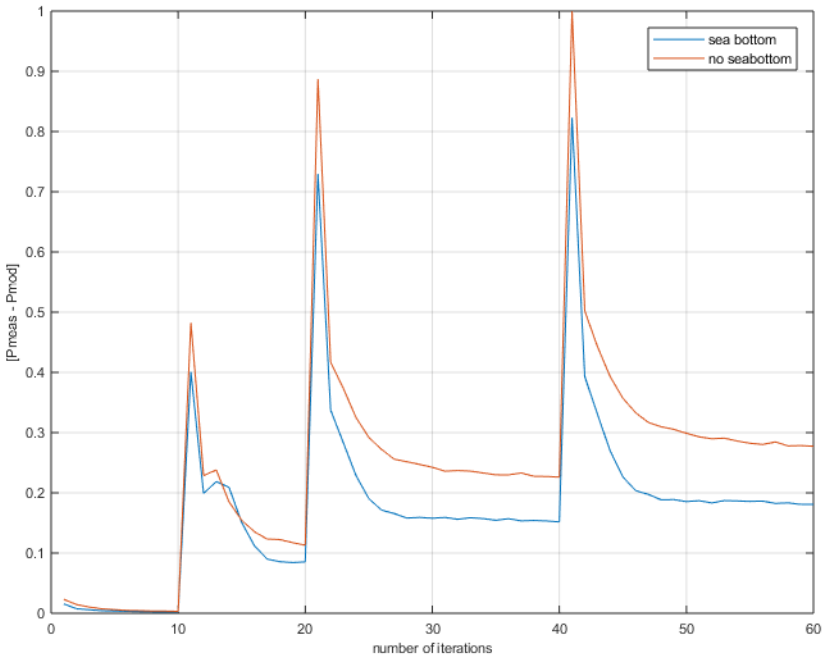

Figure 3-15: Objective functions: 400 m source spacing

Looking at the residuals at iteration 60, it is clearly visible that especially the earlier arrivals are described way better in the model using the sea bottom approach (Figure 3-16). This makes sense, because there is a lot more energy in the upper reflectors which could be described better due to correct wavefield extrapolation to the surface.

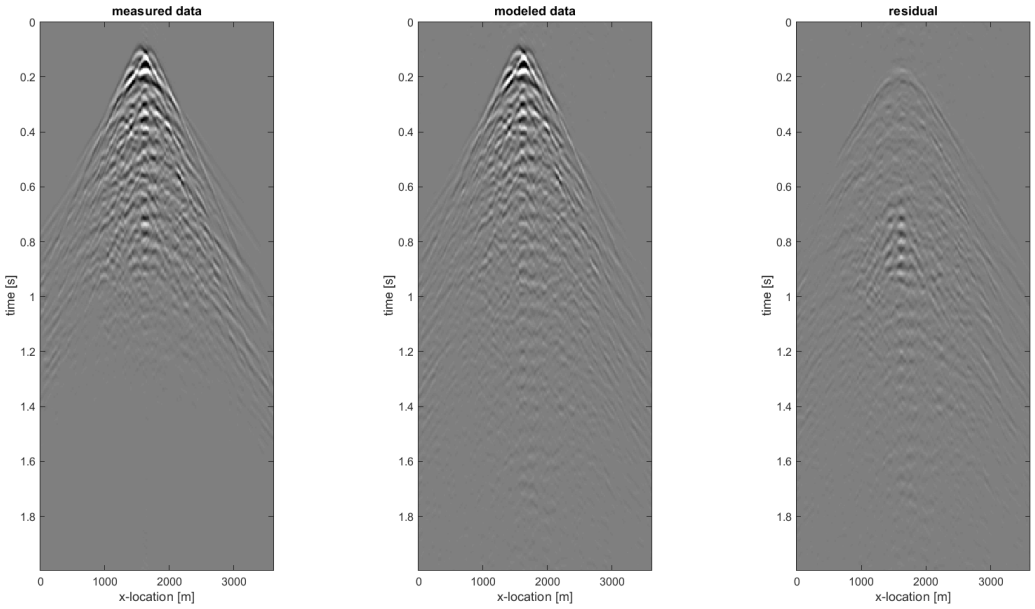

Figure 3-16: Residual sea bottom approach

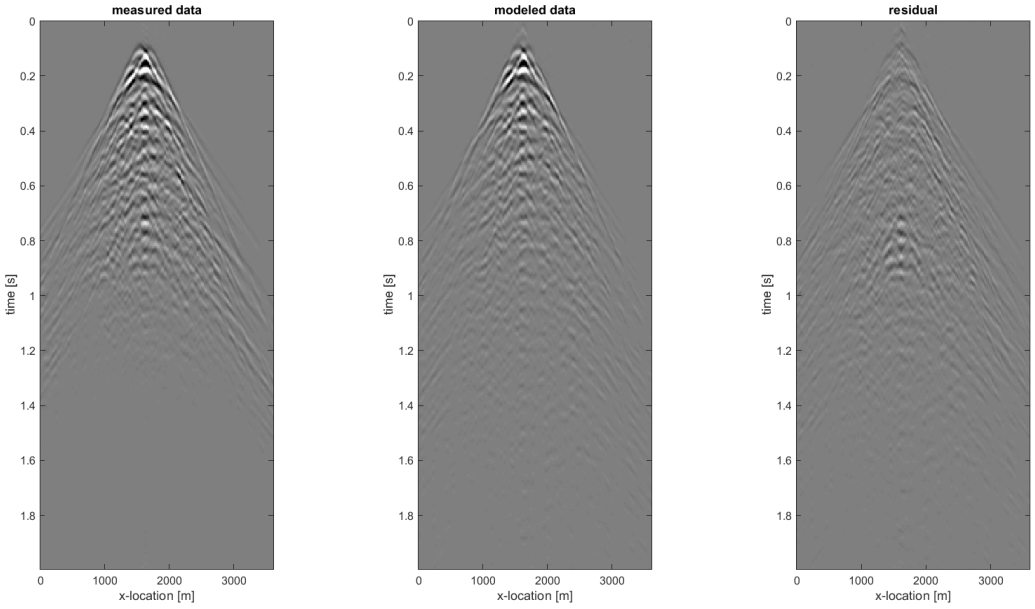

Figure 3-17: Residual no sea bottom

3-4-2 Results with sparse source and receiver spacing

In the following Figure 3-18, the result is shown for an acquisition setting using 400 m source spacing and 80 m receiver spacing. As we can see, using such an extremely sparse acquisition design, the image result suffers significantly in both images, even though using the sea bottom constraint gives a considerably better result regarding signal to noise ratio and correct imaging of the reflectors. Nevertheless it can be seen that a multiple reflection at a lateral location at around 2000 m is getting imaged as a primary and the underlying reflector at 400 m depth is not getting imaged. Observing the upper section of the image not using the proposed method, it is clearly visible that the sea bottom cannot be accurately mapped using these acquisition settings. This will of course influence the wavefield extrapolation in the full wavefield modeling to create the modeled shot gather.

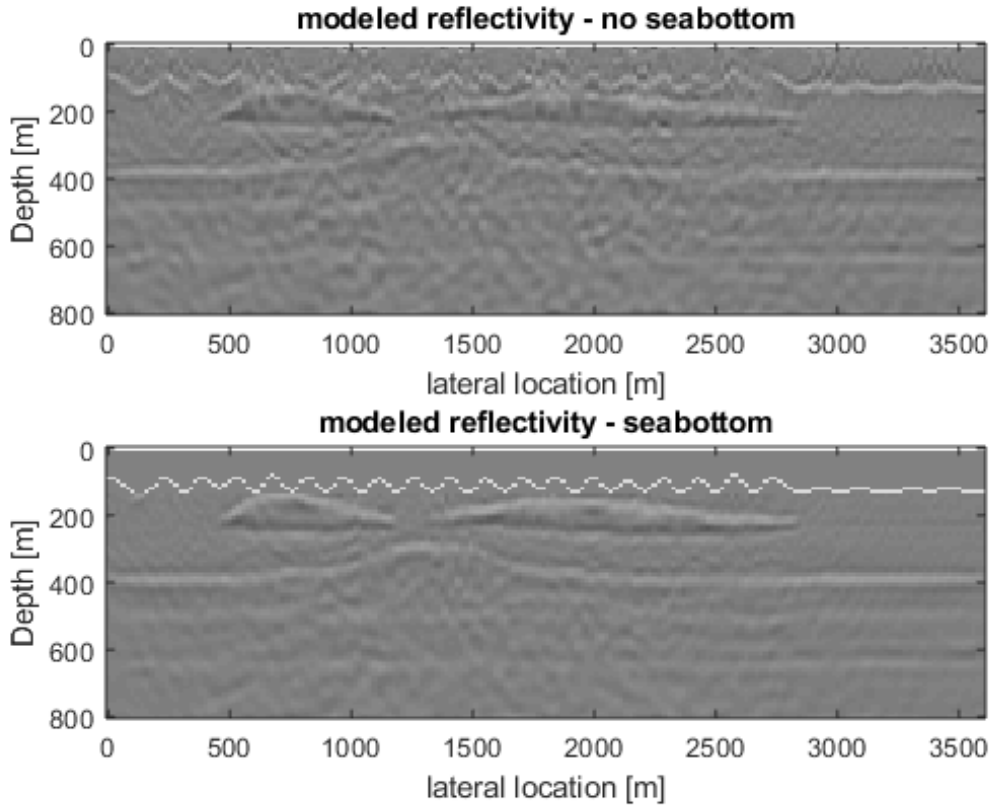

Figure 3-18: Inversion results 400 m source spacing 80 m receiver spacing

3-5 Conclusion

It could be shown that knowing the correct sea bottom topography improves the end result of the full wavefield migration significantly. A high complexity of the underlying geology combined with a chaotic sea bottom topography can heavily distort the end result of the image using full wavefield migration. Constraining the algorithm to include the sea bottom after every frequency step improves the accuracy of the wavefield extrapolation in the modeling process and therefore the measured data can be described much better with the full wavefield modeling. The lower values in the objective functions also showed that the data can be described more accurately using the proposed approach.

Furthermore we can conclude that including sea bottom topography into full wavefield migration can stabilize the imaging process especially for sparse acquisition set ups. Therefore, especially in areas where seismic data was acquired without a dense shot spacing, making use of bathymetric data can be of great value. Furthermore, sparse acquisition can lead to a much cheaper seismic surveys. Using AUVs can therefore bring cost benefits when it comes to acquiring seismic data in the future.

3-6 Discussion

This work was done by using synthetic data only. It now can be discussed, if the assumptions made in our synthetic data also hold for real scenarios. It was assumed that the exact impedance contrast from water to sea bottom is known. In a real scenario, if high quality bathymetric data was acquired by the AUV, there would be no information about lateral change of acoustic impedance of the sea bottom. It could be discussed if a shallow high frequency seismic survey would be of advantage. Due to lower frequencies and actual penetration depth into the shallow sediments, near surface anomalies as well as the lateral changes in impedance contrast of the water sediment interface can be described. Further work can then be done by including this data into the upper part of the initial model. Nevertheless, this would bear a lot higher financial resources than operating an AUV to acquire bathymetry in the area of interest.

Furthermore the data used as measured data was modeled with the same method as deployed in the inversion. This means that the data modeled from the sea bottom matches perfectly the measured data. In a real scenario this would not be the case as numerical models are just simulations with homogenizations applied, which do not truly represent the exact physical behaviour of the system. To carry out a numerical experiment that closer resembles the real world, a different model could be used in the creations of the synthetic data. Finally, the method has to be tested to field data to further inspect the potential and benefits.

Chapter 4

Final Conclusion

It can be said that bathymetric data acquired by AUVs can be valuable information for full wavefield migration. The algorithm becomes more stable, and less prone to get stuck in local minima. Furthermore it allows to do sparse acquisition which is of huge financial benefit.

It could be shown that with increasing geological complexity, a wild seafloor topography can heavily distort the final image. If this is the case, an improvement can be made by acquiring AUV data, and reprocess the vintage data with the method proposed in this thesis. The sea bottom information of seismic data could also be beneficial in order to properly navigate the AUV using the TBN algorithm.

Furthermore we can conclude that state estimation through INS and side scan measurements can lead to an improved positioning of the vehicle. Positional errors caused by errors of the INS sensors can be minimized to a certain point. Furthermore false positioning of the vehicle itself can be corrected which is not possible by only using the INS data.

Using a Kalman filter for state estimation deploying INS and sonar information during the mapping process itself, showed to lead to an effective navigation scheme.

Therefore we come to the conclusion, that the use of AUVs has great potential for aiding the seismic industry providing high quality images. Especially if a very complex sea bottom topography is present.

Bibliography

[Baysal and Sherwood, 1983] Baysal, D. D. K. and Sherwood, J. W. C. (1983). Reverse time migration. *GEOPHYSICS*.

[Berkhout, 1982] Berkhout, A. J. (1982). Seismic migration, imaging of acoustic energy by wave field extrapolation, a: theoretical aspects. *Elsevier*.

[Berkhout, 2012] Berkhout, A. J. (2012). Combining full wavefield migration and full waveform inversion, a glance into the future of seismic imaging. *GEOPHYSICS*, 77(2):S43–S50.

[Berkhout and Verschuur, 2011] Berkhout, A. J. and Verschuur, D. J. (2011). Full wavefield migration, utilizing surface and internal multiple scattering.

[Claerbout, 1971] Claerbout, J. F. (1971). Toward a unified theory of reflector mapping. *GEOPHYSICS*, 36(3):467–481.

[Davydenko, 2016] Davydenko (2016). Full wavefield migration: Seismic imaging using multiple scattering effects.

[Glynn and Buffman, 1996] Glynn, J. M. and Buffman, M. (1996). A side scan sonar system for autonomous underwater vehicles. In *Proceedings of Symposium on Autonomous Underwater Vehicle Technology*, pages 154–159.

[Hammerstad et al., 1993] Hammerstad, E., Asheim, S., Nilsen, K., and Bodholt, H. (1993). Advances in multibeam echo sounder technology. pages I482–I487 vol.1.

[Hammond and Rock, 2014] Hammond, M. and Rock, S. M. (2014). A slam-based approach for underwater mapping using auvs with poor inertial information. pages 1–8.

[Kalman, 1960] Kalman, R. E. (1960). A new approach to linear filtering and prediction problems. *Journal of Basic Engineering*, 82(1):35.

[Sintes, 2002] Sintes, C. (2002). Interferometric side scan sonar : A tool for high resolution sea floor exploration.

[Taraldsen et al., 2011] Taraldsen, G., Reinen, T. A., and Berg, T. (2011). The underwater gps problem. pages 1–8.

[Tarantola, 1985] Tarantola (1985). Inversion of seismic reflection data in the acoustic approximation.

[Tsingas et al., 2017] Tsingas, C., Al-Ali, M., Walker, C., Bunting, T., Postic, E., Rokkan, A., Valsvik, G., and Brizard, T. (2017). Spicerack: An autonomous underwater vehicle for efficient seabed seismic acquisition.